

A Galaxy Model from 2MASS Star Counts in the Whole Sky Including the Plane

P. Polido¹ and F. Jablonski²

Divisão de Astrofísica, Instituto Nacional de Pesquisas Espaciais, Avenida dos Astronautas 1758, 12227-010 São José dos Campos SP, Brazil

and

J. R. D. Lépine³

Instituto de Astronomia, Geofísica e Ciências Atmosféricas, Universidade de São Paulo, Rua do Matão 1226, 05508-900 São Paulo SP, Brazil

ABSTRACT

We use the star counts model of Ortiz & Lépine (1993) to perform an unprecedented exploration of the most important galactic parameters comparing the predicted counts with the 2MASS observed star counts in the J, H and K_S bands for a grid of positions covering the whole sky. The comparison is made using a grid of lines-of-sight given by the HEALPix pixelization scheme. The resulting best fit values for the parameters are: (2120 ± 200) pc for the radial scale length and (205 ± 40) pc for the scale height of the thin disk, with a central hole of (2070_{-800}^{+2000}) pc for the same disk; (3050 ± 500) pc for the radial scale length and (640 ± 70) pc for the scale height of the thick disk; (400 ± 100) pc for the central dimension of the spheroid, (0.0082 ± 0.0030) for the spheroid to disk density ratio, and (0.57 ± 0.05) for the oblate spheroid parameter.

Subject headings: Galaxy: fundamental parameters — Galaxy: structure — infrared: stars — stars: statistics

1. Introduction

The star counts method is an important tool for the investigation of the galactic structure and is based on the equation of stellar statistics (Binney & Merrifield 1998):

$$N_s(m_1, m_2, l, b) d\Omega = \int_{m_1}^{m_2} dm \int_0^\infty r^2 dr \rho_s(r, M) \phi_s(M) d\Omega, \quad (1)$$

which allows us to predict the number of objects for a certain line-of-sight defined by the galactic longitude l and the galactic latitude b . N_s is the number of stars of type s with apparent magnitude between m_1 and m_2 in a solid angle $d\Omega$ in

the direction defined by (l, b) ; r is the heliocentric distance, ρ_s is the stellar density and ϕ_s is the luminosity function. We adopted the luminosity function as the number of stars per cubic parsec near the Sun with magnitudes in the range $(M, M + dM)$. It is convenient to handle the stellar densities normalized with respect to the values in the solar neighborhood.

The star counts models can be classified in roughly two categories: those adopting an empirical luminosity function – based on observations of the stellar populations in the solar neighborhood and specific environments, like globular clusters – and those adopting a luminosity function derived from theoretical stellar evolutionary tracks and the associated distributions of stellar masses, ages and metallicities. The pioneer investigation of Bahcall & Soneira (1980) fits into

¹pripolido@gmail.com

the first group, together with models like the ones by Wainscoat et al. (1992), Ortiz & Lépine (1993) (hereafter OL93), Jurić et al. (2008) and Chang et al. (2011). On the other hand, the works of Robin & Crézé (1986) and Girardi et al. (2005) belong to the group of models which adopt a stellar evolution approach to define the luminosity function.

The number of components used to represent the Galaxy varies from model to model, according to the focus of the work. Basically, two components are always present: a disk and a spheroid. After Gilmore & Reid (1983) many authors adopted the disk component consisting of a thin disk and a thick disk. Concerning the spheroid, despite this terminology being used in all models, it actually may indicate different galactic structures, like the bulge, the halo or even both (e.g., OL93). The densities of stars on the disks decrease exponentially with galactocentric radius and with the vertical distance to the plane, whereas the density in the spheroid follows a decay similar to the de Vaucouleurs' law.

Despite strong evidence that our galaxy has a spiral structure, the number of arms, as well as the parameters which describe their shapes and positions vary from work to work (e.g., Russeil (2003); Levine et al. (2006); Vallée (2008); Hou et al. (2009)). The star counts models which attempt to take the spiral arms into account are those due to OL93 and Wainscoat et al. (1992).

The existence of a bar in the central region of our galaxy was proposed in the 1970s based on the large non-circular motions seen in the observations of HI and CO in the inner Galaxy (Peters 1975; Cohen & Few 1976; Liszt & Burton 1980), but only in the 1990s the combination of evidences such as the NIR light distribution (Blitz & Spergel 1991; Weiland et al. 1994), star counts asymmetries (Nakada et al. 1991; Stanek et al. 1997; Benjamin et al. 2005), gas kinematics (Binney et al. 1991; Englmaier & Gerhard 1999; Fux 1999) and large microlensing optical depth (Udalski et al. 1994; Zhao et al. 1995; Han & Gould 1995) became more persuasive.

Bahcall & Soneira (1980) examined the star counts in the BV bands and assumed that the Galaxy could be well represented by two components: a disk and a spheroid. Robin & Crézé (1986) examined the star counts in the UBV bands and used three components to model the Galaxy:

a disk, a halo and an exponential spheroid population with intermediate age. Wainscoat et al. (1992) adopted five components (disk, halo, bulge, spiral arms, molecular ring) to model the Galaxy star counts as a foreground for their extragalactic source counts based on Infrared Astronomical Satellite Survey (IRAS)¹. OL93 attempted to model the star counts in RIJHKL, [12 μ m] and [25 μ m] IRAS bands, using four components: a spheroid, two disks with scale heights 100 pc and 390 pc, and spiral arms. A version of the model with an intermediate disk and a bar is described in their website². The approach of Girardi et al. (2005) uses a stellar populations synthesis code as the input for the luminosity function to compare their four components model (thick disk, thin disk, halo, bulge) with optical and infrared data, including the Two Micron All Sky Survey (2MASS)³, Chandra Deep Field South (CDF5) and Hipparcos⁴. Jurić et al. (2008) have compared the stars counts from the Sloan Digital Sky Survey (SDSS)⁵ with the predicted counts from their galactic model with a disk and a halo. Chang et al. (2011) used a model with a spheroid and a disk, and a power-law luminosity function for which the power index is a free parameter at each grid point on the sky for galactic latitudes $|b| > 30^\circ$. The comparison was made for 8192 lines-of-sight in the 2MASS K_S band.

In this study we use the homogeneous all sky coverage of the 2MASS to test the OL93 model in the JHK_S bands. We explore the parameters space of this model adopting an updated luminosity function to describe the stellar populations in the solar neighborhood.

In sections 2 and 3, we describe the OL93 model and the method used to search for the best fit parameters. The results and discussion are presented in section 4. Our conclusions follow in the last section.

2. The Galactic Model

The OL93 model uses a young disk, an old disk, an intermediate disk composed of C-stars,

¹<http://irsa.ipac.caltech.edu/Missions/iras.html>

²<http://www.astro.iag.usp.br/~jacques/pingas.html>

³<http://www.ipac.caltech.edu/2mass/>

⁴<http://www.rssd.esa.int/Hipparcos/>

⁵<http://www.sdss.org/>

a spheroid, spiral arms and a bar, with the total number density of sources being the sum of all individual contributions. A detailed description of all components follows.

2.1. Disks

We consider a thin (young) disk and a thick (old) disk. The density of each subcomponent $i = Y(\text{oung}), O(\text{ld})$, is given by a modified exponential (Lépine & Leroy 2000), which is an important change with respect to the original model:

$$n_{d,i}(r, z, s) = n_{d,i}(R_0, 0, s) e^{-\frac{r}{\alpha_i} - \frac{\beta_i}{r} - \frac{z}{h_i(r)}}. \quad (2)$$

Here r is the distance to the galactic center in the plane of the Galaxy, $n_{d,i}(R_0, 0, s)$ is the star density of spectral type s in the solar neighborhood, α_i is the radial scale length, which does not depend on the spectral type, $h_i(r)$ is the scale height and β_i is the radius of a hole in the central part of the disk. The thick disk has a distribution of spectral types of giants similar to that found in globular clusters. All the stars of spectral types O and B, as well as the supergiants of all spectral types were excluded from the composition of the thick disk. The scale height $h_i(r)$ is given by:

$$h_i(r) = z_i e^{\frac{0.4(r-R_0)}{R_0}}, \quad (3)$$

where z_i is the scale height in the solar neighborhood. The free parameters of the model related to the disks are $\alpha_Y, \alpha_O, \beta_Y, \beta_O, z_Y$ and z_O .

Recent studies (e.g., Sofue et al. (2009) and Amôres et al. (2009)) suggest the existence of a minimum in the density of young objects in the solar neighborhood due to the effects of corotation of the spiral pattern with the galactic rotation. We experimented with this possibility modeling the young disk density with

$$n_{d,Y}(r) = n_{d,Y}(R_0) \left[1.3 - 0.3e^{-(r-R_0)^2} \right], \quad (4)$$

where r and R_0 are expressed in kpc. The results of this attempt are shown in section 4.2.1.

OL93 also consider an intermediate disk consisting of carbon stars which are bright in infrared mainly during their Asymptotic Giant Branch (AGB) phase, when they lose mass at high rates.

This component does not show radial dependence (Guglielmo 1998) but its density decreases exponentially with the distance to the galactic plane with a scale height of 200 pc. We did not attempt determining any parameter related to this component.

The OL93 model does not use warp components on the disks. Evidences for the presence of this contribution in 2MASS data are presented by López-Corredoira et al. (2002) and Reylé et al. (2009). Uncertainties related to the different space distributions of dust and stars (Freudenreich et al. 1994; Drimmel & Spergel 2001; Reylé et al. 2009) and differences in the distribution of giant and main sequence stars (eg. López-Corredoira et al. (2002)) led us not to attempt including this component in our modeling.

2.2. Spheroid

The spheroidal structure is subtle, and when we observe it, specially close to the galactic center, we see the superimposition of contributions from the young and old disks (which may or may not have central holes), and a galactic bar. Besides, the innermost regions of the spheroid are subject to heavy reddening. A number of improvements to the description of this region as a whole have been suggested in the last decade. López-Corredoira et al. (2005) found that the best fit to 2MASS data is given by a structure which consists of a boxy bar associated to a tri-axial bulge. Vanhollebeke et al. (2009) also use a tri-axial figure which is truncated by a Gaussian decay, and Robin et al. (2012) describe the 2MASS data in the central region of the galaxy ($|l| < 20^\circ, |b| < 10^\circ$) with a triaxial boxy bar/bulge plus a longer and thicker ellipsoid. Nataf et al. (2013), McWilliam & Zoccali (2010) and Saito et al. (2011) investigated the X-shaped component which is part of the bar/bulge structure.

The OL93 model uses an oblate spheroid in an attempt to describe both the inner region and larger outer scales. The density in the spheroid is adapted from the mass density of Hernquist (1990) and is given by:

$$n_{sph}(R, s) = \frac{C_1}{\zeta(\zeta + a_H)^3}, \quad (5)$$

where R is the distance to the galactic center, $\zeta = \sqrt{(z/\kappa)^2 + R^2}$, with κ being the oblateness

of the spheroid and z the distance above the galactic plane. a_H is a scale length, and $C_1 = R_0(R_0 + a_H)^3(N_{sph}/N_D)$. The last term is the ratio of densities of spheroid and disk populations in the solar neighborhood. R_0 is the distance of the sun to the galactic center, taken here as 8.0 kpc – very close to both arithmetic and weighted means of R_0 determinations obtained since 1992 (Malkin (2013); Morris et al. (2012); Reid (2012, 2013); Zhu & Shen (2013)). OL93 used $R_0 = 7.9$ kpc, which was intermediate between the IAU recommended 8.5 kpc and the “short scale” value 7.5 kpc often used at the time (see for instance a discussion in Section 2 of Lépine et al. (2011)). The stellar population of the spheroid is considered the same as that of the thick disk, discussed below. a_H , κ and N_{sph}/N_D are free parameters in the OL93 model.

2.3. Spiral arms

One of the first representations of the spiral structure in the Milky Way, due to Geogelin & Geogelin (1976), proposed a four arms pattern. Since then, many authors have studied this galactic component, obtaining discrepant results for the number of arms and their locations. Recent results include Majaess et al. (2009), based on the space distribution of type II Cepheids which suggest deviations from what logarithmic spirals predict for the Sagittarius-Carina arm and the Local arm. Lépine et al. (2011) traced the CS molecular emission related to IRAS sources and concluded that they are not fitted by logarithmic arms, rather by a sequence of straight line segments. From 2MASS data and gas distributions, Francis & Anderson (2012) concluded that the Milky Way is a two-armed grand-design spiral. Robitaille et al. (2012) found the existence of two dominant and two secondary arms on GLIMPSE, MIPS GAL and IRAS data. In the outer parts of the Galaxy the spiral arms are not very prominent. Quillen (2002) even suggested, based on 2MASS data, that the Galaxy is flocculent in that region. Comprehensive reviews of earlier works can be found in Vallée (1995, 2002, 2005).

The spiral pattern is the same as in the OL93 model, with four logarithmic arms, each described by:

$$r_{arm} = qe^{(\theta - \theta_0)\tan(i)}, \quad (6)$$

where q is the galactic radius where each arm begins, θ_0 is the initial galactocentric angle and i is the pitch angle. The arms are confined to the range of galactic radii 2 kpc $< r < 15$ kpc and consist of O5-B stars of all luminosity classes and supergiants of all spectral types. We adopted an improved version of the OL93 arms configuration, consistent with recent observations. Values for q , i and θ_0 were derived from the fit of Equation 6 to the representation seen in Churchwell et al. (2009) which is based on the model of Geogelin & Geogelin (1976) with some modifications: variations in positions according to results of parallax distances to masers in regions of stellar formation (Xu et al. 2006); refinement in the tangential directions to the arms from CO surveys (Dame et al. 2001); revisions in the amplitudes of the arms due to GLIMPSE results and the work of Drimmel & Spergel (2001); and finally, the locations of the outer and distant arms using kinematical data (McClure-Griffiths et al. 2004).

The only parameter related to the spiral pattern which we attempted to derive from the 2MASS observations is the density contrast between the arms and the thin disk, C_S , since the arms behave as enhancements of the disk density. The stars density perpendicular to the arm’s length is described by a Gaussian function and its half width at half maximum is taken as ~ 180 pc. The tangential directions to the arms, which are also the directions where we expect to see the largest contribution of the arms to the star counts, are located at longitudes 32° , 49° , 284° and 308° .

2.4. Bar

Prior information on the structural properties of the bar is somewhat sparse. It is generally accepted that our galaxy has a bar, but its length, shape and orientation cover wide ranges in the literature. The half length of the bar, for example, ranges from 0.67 kpc in Cao et al. (2013) to 3.9 kpc in López-Corredoira et al. (2007).

In our modeling, the bar contribution to the stellar density is given by:

$$r_{bar} = \left\{ \left[\left(\frac{x'}{x_0} \right)^2 + \left(\frac{y'}{y_0} \right)^2 \right]^2 + \left(\frac{z'}{z_0} \right)^4 \right\}^{\frac{1}{4}}$$

$$n_{bar} = (n_{d,Y} + n_{d,O})C_{bar} e^{-\frac{1}{2}r_{bar}^2} \quad (7)$$

where r_{bar} describes the shape (x', y', z' are along the three axes) and C_{bar} gives the contribution of the bar relative to the sum of the disk densities (Dwek et al. 1995). We explored axes ratios in the ranges $\{x_0 : y_0 : z_0\} = \{1.00 : (0.22 - 0.67) : (0.34 - 0.40)\}$ and x_0 up to 4 kpc, a little more than the largest value found in the literature (López-Corredoira et al. 2007). The orientation of the bar with respect to the line Sun-GC, θ_{bar} , was allowed to be in the range $11^\circ - 53^\circ$. Even though not strongly constrained by the 2MASS data, we attempted to determine the geometrical parameters of the bar as well as the density contrast between the bar and the disks.

2.5. Interstellar extinction

The interstellar extinction is an important ingredient of a galactic model, specially in the galactic plane. Due to the accumulation of dust in the galactic plane, the extinction is larger in this region of the Galaxy. The model of Amôres & Lépine (2005) is based on the distribution of gas (HI and CO) and interstellar dust (IRAS 100 μm), under the assumption that the dust is well mixed with the gas. In this model, the Galaxy has axial symmetry, the gas density varies radially in a smooth way and the spiral arms produce no effects in the extinction. The interstellar extinction is calculated assuming that it is proportional to column density of hydrogen, in both atomic (N_{HI}) and molecular (N_{H_2}) forms:

$$A_V = C_V(r)N_{HI}(R, z) + 2C_V(r)N_{H_2}(R, z). \quad (8)$$

Here C_V is a proportionality factor, with average value of 5.3×10^{-22} mag cm^2 (Bohlin et al. 1978), if $A_V = 3.1E_{B-V}$, but it can change along the galactocentric radius due to the metallicity gradient. For galactocentric distances in the plane with $r > 1.2$ kpc, the authors suggest a proportionality with $r^{-0.5}$. For $r < 1.2$ kpc, due to the highly uncertain metallicity of the region, a constant value is employed. Similar analytical expressions were adopted for both gas forms:

$$n_{HI, H_2} = ce^{-\frac{r}{a} - \left(\frac{b}{r}\right)^2}, \quad (9)$$

where, for HI, $a = 7$ kpc, $b = 1.9$ kpc and $c = 0.7 \text{ cm}^{-3}$, and for H_2 , $a = 1.2$ kpc, $b = 3.5$ kpc and $c = 58 \text{ cm}^{-3}$. Since there is a large concentration of H_2 in the galactic center, for $r < 1.2$ kpc this was modeled separately with the function

$$n_{H_2} = de^{-\left(\frac{r}{f}\right)^2}, \quad (10)$$

with $f = 0.1$ kpc and $d = 240 \text{ cm}^{-3}$.

The vertical distribution of hydrogen is given by a Gaussian function of z :

$$n_H(r, z) = n_H(r)e^{-\frac{1}{2}\frac{z^2}{(1.18z_{1/2})^2}}, \quad (11)$$

where $z_{1/2}$ is the half width at half height of the scale height. Amôres & Lépine (2005) suggest for the scale height of H_2 :

$$z_{1/2} = 45e^{0.1r} \text{ pc}, \quad (12)$$

while for HI the same expression must be multiplied by a factor 1.8.

2.6. Luminosity function

The luminosity function used in this work follows OL93 and enters the code via a table containing up to 64 classes of objects among main sequence, giants, supergiants and variable objects. The space densities were updated to be consistent with recent results. Figure 1 shows the luminosity function for main sequence and giant stars according to OL93, Wainscoat et al. (1992), Bochanski et al. (2010), Reid & Gizis (1997) and Murray et al. (1997). The luminosity functions for supergiants and variable objects are the same as in OL93.

3. Methodology

3.1. The data: star counts from the 2MASS catalog

Since interstellar extinction is lower in the near infrared (NIR), surveys in this region are efficient to investigate the structure of the Galaxy. The 2MASS project (Skrutskie et al. 2006; Cutri et al. 2003) covers 99.8% of the sky in the NIR with 471 million point sources observed in J (1.25 μm), H (1.65 μm) and K_S (2.17 μm). At SNR=10, the limit magnitudes for point objects are 15.8, 15.1 and 14.3 in the J, H and K_S bands, respectively. These limits refer to unconfused sources outside

the galactic plane ($|b| > 10^\circ$) and far from areas where the interstellar extinction is large. The all-sky coverage of the 2MASS data allows us to make a comprehensive comparison of the observed counts with the predictions of the model by OL93.

The number of sources in a given line-of-sight through the Galaxy can be obtained from the 2MASS database in three forms: cone, box and polygon search. Taking into account practical aspects such as the elapsed time for retrieving the data, we opted to use the cone search, with a cone area of one square degree. We use a grid of galactic longitudes and latitudes as generated by the Hierarchical Equal Area Isolatitudes pixelization of the Sphere (HEALPix)⁶ (Górski et al. 2005) in order to obtain a uniform sampling in galactic coordinates. The orientation of the grid is such that the “equator” of the HEALPix scheme coincides with the galactic plane. Our basic grid contains 192 points (the N_{side} parameter of HEALPix = 4). A $N_{side}=8$ grid (768 points) was used to provide four neighbors to each point of the $N_{side}=4$ scheme in order to estimate the variance of the star counts at each position of the basic grid. This allows us to verify if the assumption of using a \sqrt{N} law for the uncertainty in the counts, N , is reasonable. It turns out that the dispersion obtained from the five points estimate is consistent with the Poisson uncertainties for most of the sky, but significant differences show up close to the galactic plane. This simply reflects the structure of the Galaxy in a scale of a few degrees and the large gradients in star counts along the z direction close to the galactic plane. We investigated the results of using one or other option for the uncertainties in the observed star counts and the results are shown in section 4.

The output of a cone search is a list of JHK_S magnitudes and catalog flags for each counted object. The flags include important indicators to eliminate low quality counts. We examined the following flags: photometric quality, read flag, contamination and confusion flag, and galactic contamination (extended objects) flag. Table 1 summarizes the criteria to consider a source *bad*. Table 2 summarizes the percentage of rejections for a few lines-of-sight. One can see that even far from the galactic plane, the K_S band is more prone

to be affected by rejections than the other bands, while in regions near the galactic plane the three bands have about 50% rejections. This indicates that comparisons in the galactic plane should not go to magnitudes fainter than 11. Using an extreme field as an example ($l = 11.25^\circ, b = 0.0^\circ$), at the 11th magnitude bin we find 74 rejections out of a total of 1062 counts for the J band, 566 (in a total of 4860) for the H band and 2076 (in a total of 9990) for the K_S band (7%, 11.6% and 20.8%, respectively). The fractions of rejections are 25 to 30% from photometric quality, 10-15% from the read flag and 65-75% from the contamination/confusion flag.

The limiting magnitude varies from grid point to grid point due to differences in interstellar extinction and to the existence of non-resolved close sources. This is specially true for regions in the galactic plane and close to the galactic center. To set up a limiting magnitude for each grid point we stepped in magnitude, counting the corresponding objects and monitoring the number of associated rejections. The limiting magnitude was set when the fraction of rejected objects reached 10%.

Objects not rejected are put into ascending order of magnitude in each band and the cumulative star counts are obtained from the sums up to a certain limit magnitude. The differential counts can be obtained from the latter.

3.2. Parameters estimation

Models in which multiple parameters are to be evaluated are recognizably challenging, in the sense that traditional methods of search for an optimal solution, like those based on gradients in the figure of merit (e.g., the Downhill Simplex method of Nelder & Mead (1965)) may lead to local maxima (or minima) which can be far from the best solution. A number of statistical methods has received attention in the last decades because even though being relatively slow, they produce reliable results. We chose to use the Markov chain Monte Carlo method to have an overall view of the parameter space, including a rough localization but with a reliable measure of the spread of the parameters, and the Nested Sampling (NS) method to have a better estimate of the parameter values. We experimented with MCMC chains of up to 10^5 iterations to have an overview of possible multiple modes in parameter space. Our conclu-

⁶ <http://healpix.jpl.nasa.gov/>

sion is that with typically 10^4 iterations one can unambiguously limit the region of interest for each parameter. The NS procedure subsequently progresses faster to the mode, in some cases with only a few hundred iterations.

3.2.1. MCMC

Markov chain Monte Carlo (MCMC) (Gilks et al. 1996) is probably the preferred first approach for an overall view of the parameter space in a multi-parameter problem. It has the virtue of being very simple to code and provides a first assessment of the location and spread of the parameters. It is perfectly suited for the Bayesian context, where prior information may be relevant in parameter estimation or model selection. Briefly, if we have a set of data D with individual points d_1, d_2, \dots, d_N and a model M with a vector of parameters $\theta_1, \theta_2, \dots, \theta_{N_p}$, for which we are able to calculate the likelihood \mathcal{L} , the MCMC algorithm progresses as follows.

1. Consider an initial state θ , randomly chosen, with associated likelihood \mathcal{L} .
2. Draw a random candidate state θ^* , statistically centered on θ , for which the likelihood is \mathcal{L}^* .
3. Calculate the ratio $\alpha = \frac{\mathcal{L}^*}{\mathcal{L}}$
4. if $\alpha > 1$
 accept the new state
 else
 draw a random number β in $[0, 1]$
 if $\beta < \alpha$
 accept the new state
 else
 stay in the old state
5. Record the chosen state and continue at step 2.

Since we considered flat priors for all parameters, the histograms of the chain for each parameter may be regarded as proportional to the *a posteriori* distribution of the parameter. Each histogram location gives us an estimate of the value of the parameter itself and the confidence region (or uncertainty) may be obtained by integrating the area (for example, the one corresponding to

the 1- σ quantile in a normal distribution) around the mode or the median of the histogram.

By far step 2 in the scheme above is the most involving, since it implies defining a *step size* by which to statistically draw the proposal states θ^* . Suppose a particular parameter h . As for all other variables, we work on normalized quantities (here h_n) calculating $h_n = (h - h_{min}) / (h_{max} - h_{min})$ and then draw the proposal $h_n^* \sim \mathcal{N}(h_n, 0.289\Delta)$. Here “ \sim ” means “distributed as”. The numerical factor 0.289 ensures that the step variance is similar to the variance generated by the step Δ in a uniform distribution. With this scheme, all normalized variables are subject to the same step size. We follow the recommendations in the literature (e.g., Sivia & Skilling (2006)) and tune Δ as the chain progresses to have an acceptance rate of $\sim 37\%$. The initial value of Δ is 0.25, and the adaptive scheme for changing its size is only started after 2^{N_p} steps of the chain, to allow for exploration of distant regions in parameter space.

We investigated two forms for the likelihood \mathcal{L} . In the first, we calculate for the whole grid of n_{pix} lines-of-sight (in one band, say H),

$$\chi_{\text{H}}^2 = \frac{1}{n_{pix}} \sum \frac{1}{N_b} \sum_{j=m_l}^{m_u} \frac{(C_{obs,j} - C_{M,j})^2}{(C_{obs,j} + C_{M,j})}. \quad (13)$$

Here $C_{obs,j}$ are the 2MASS observed counts in each line-of-sight, with j running from the lower magnitude limit m_l to the upper magnitude limit m_u and $C_{M,j}$ are the corresponding model quantities. Each line-of-sight has a cumulative histogram of $N_b = ((m_u - m_l) / \Delta m) + 1$ magnitude bins. The other bands are treated similarly, and we finally write for the likelihood

$$\mathcal{L} \propto \exp\left(-\frac{1}{2}\chi^2\right) \quad (14)$$

with $\chi^2 = \chi_{\text{J}}^2 + \chi_{\text{H}}^2 + \chi_{\text{Ks}}^2$.

Since Equation 14 assumes that the C_{obs} terms in Equation 13 are statistically independent and normally distributed – and the latter is not the case for low counts – we also used the Poisson likelihood form prescribed in Bienayme et al. (1987) and Robin et al. (1996):

$$\ln \mathcal{L} = \sum_{j=m_l}^{n_{pix}} \sum_{m_u} C_{obs,j} (1 - \zeta_j + \ln \zeta_j), \quad (15)$$

where $\zeta_j = \frac{C_{M,j}}{C_{obs,j}}$.

The two likelihood forms allow us to perform a sanity check on the results since Equation 13 gives more weight to instances of large star counts while Equation 15 attributes equal weights to the counts in all magnitude bins. The largest difference in parameter values, however, is small, typically less than 5%. The median of the absolute value of the relative residuals, $((C_{obs,11} - C_{M,11})/C_{M,11})$, in a grid of 3072 lines-of-sight is typically less than 2%.

3.2.2. Nested Sampling

Nested Sampling (NS) is an algorithm for optimization in multi-parameter problems invented by Skilling (2004). It relies on the idea that whatever the number of parameters in a model, we can always populate the parameter space with a number N_{live} of random samples and calculate their likelihoods. Instead of focusing on the best likelihoods, the algorithm works on the worst. Our implementation of NS is as follows:

1. Populate the parameter space with N_{live} samples chosen randomly. Notice that a minimum minimorum choice for N_{live} would be 2^{N_p} , where N_p is the number of parameters being sought. Calculate the associated \mathcal{L}_i , $i = 1, \dots, N_{live}$. The associated $j = 1, \dots, N_p$ parameters are stored in the vectors $\theta_{i,j}$
2. Find the *worst* \mathcal{L} among the N_{live} \mathcal{L}_i and call it $\mathcal{L}^* = \mathcal{L}_{i_{worst}}$
3. Choose at random an index k among $1, \dots, N_{live}$ such that $k \neq i_{worst}$
4. Explore the vicinity of point θ_k with a short MCMC, and choose from its output a parameter set θ_{copy} for which $\mathcal{L} > \mathcal{L}^*$
5. Substitute $\theta_{i_{worst}}$ with θ_{copy} and jump to step 2.

A simple scheme for stopping the NS algorithm was set based on the size of the MCMC proposal

step in item 4 above. When $\Delta < 0.0001$, we finish the iterations. Again, Δ is allowed to vary only after 2^{N_p} steps of the NS algorithm.

The limits we adopted for parameters search are shown in Table 3. They were chosen so to cover with some slack the range of values found in the literature.

3.3. Finer search for selected parameters

The $N_{side}=4$ HEALPix grid provides a good first assessment of the galactic parameters but has the obvious limitation of being too coarse, specially in regions close to the galactic center. To circumvent that, we did several experiments with finer grids, for which only a few parameters were explored. For example, a grid of 382 lines-of-sight drawn from $N_{side}=16$ HEALPix scheme provides a good coverage of the central region of the galaxy and is not very expensive in terms of computing time. At $l = b = 0^\circ$ it samples every 5.6° in longitude and 2.4° in latitude. In order to probe also regions far from the galactic center, the 382 points are drawn from the $N_{side}=16$ scheme according to the density of star counts. Figure 2 illustrates the $N_{side}=4$ basic grid and also the finer grid drawn from the $N_{side}=16$ scheme.

The previously well determined parameters, α_Y, α_O, z_Y and z_O are little affected by the choice of a finer grid. However, a_H and N_{sph}/N_D are. This is due to the fact that the cusp in star counts clearly visible at $-10^\circ < l < +10^\circ$ is well sampled by the finer grid. The trend of the changes is in the sense that a_H falls and N_{sph}/N_D goes up.

4. Results

4.1. Parameters

Figure 3 shows an overview of the joint distributions of probabilities of the parameters from a MCMC run of 10^5 iterations considering the $N_{side}=4$ HEALPix grid. One can see that α_Y, α_O, z_Y and z_O are the best constrained parameters, followed by N_{sph}/N_D and κ . Two factors contribute for making the estimates of a_H, β_Y , and β_O more difficult: their much more subtle contribution to the overall behavior of the counts and the relatively poor resolution of the 192 points grid. One has to recall that the separation of samples in longitude for $b = 0^\circ$ is 22.5° , and that the

first “parallels” are at $|b| \sim 9.6^\circ$. The parameter related to the contrast of the spiral arms, C_S , and the parameters of the bar ($C_{bar}, \theta_{bar}, x_0, y_0, z_0$) were kept fixed at the best possible guesses when using the sparse grid. This means contrasts of the order of the unity, $\theta_{bar} \sim 30^\circ$, $x_0 \sim 2000$ pc and $\{x_0 : y_0 : z_0\} = \{1.0 : 0.4 : 0.4\}$.

Figure 4 illustrates our attempt to better constrain the parameters via the NS algorithm. For $\alpha_Y, \alpha_O, z_Y, z_O$ and N_{sph}/N_D the best solution coincides well with the maximum likelihoods from the MCMC run. For $\beta_Y, \beta_O, a_H, \kappa, C_S$ and C_{bar} the maxima tend to fall in regions that may be far from the correspondent in the MCMC distribution. This just reflects the “flat” nature of the likelihood landscape, with small differences between the discrete evaluations which can lead to solutions along a wide range of values. We tried to mitigate this limitation choosing as the start state for the NS algorithm 32 random likelihoods among the 5% best evaluated in a MCMC run of 25000 steps. The result is shown in Figure 5. We see that the best determined parameters from the MCMC procedure converged to consistent values, while the rest tend – even though converging to definite values – to show substantial spread in parameter space as the NS algorithm progressed.

Table 4 summarizes the results shown in Figs. 3, 4 and 5 in numerical form. The well constrained parameters, α_Y, α_O, z_Y and z_O , show consistency in all three approaches and are probably more accurately determined than indicated by the MCMC procedure alone. For the rest of the parameters the range indicated by the MCMC exploration is large and reflects the weak constraints imposed on them by the adopted sampling grid.

Table 5 shows the effects of adopting different uncertainties in the star counts as mentioned in Section 3.1. To make the comparison simple, we chose to minimize only the well determined parameters. As one can see, the different weighting schemes do not produce conflicting results. In the following, we discuss only results for which the \sqrt{N} scheme was used.

The adoption of a finer grid (see Section 3.3) improves our ability in determining parameters that are related to spatially limited regions of the Galaxy. This is the case for the spheroid, for example. Figure 6 shows the result of a MCMC on such a finer grid. Notice that we fixed ill-

determined parameters like β_O, C_S and C_{bar} to the best possible guesses. A further NS run on the region constrained by the MCMC run of Figure 6 using the full resolution of a $N_{side} = 16$ (3072 points) grid, provided us with what we consider the best estimate for the basic galactic parameters from the 2MASS data. They are discussed in the following section.

4.2. Comparison with results in the literature

Table 6 shows the results of this work together with a compilation of corresponding values found in the literature, to facilitate a comparison and discussion of possible differences. The first result that catches our attention is α_Y , for which we obtain values which are systematically smaller than those quoted in the literature, specially considering the results from the $N_{side} = 4$ coarse grid. We attribute at least part of the difference to the interplay between α_Y and β_Y – the latter in general not used in models by other authors. α_O is comparable with the estimates of Larsen & Humphreys (2003) and Chang et al. (2011). Like in most cases seen in the literature, we found that α_O is larger than α_Y . López-Corredoira et al. (2002) present parameters for the galactic disk also based on 2MASS data. They found 2.1 kpc for the scale length of the disk, which is in agreement with what we found for the thin disk. The value we obtain for β_Y is consistent with the estimates by Freudenreich (1998), Lépine & Leroy (2000), López-Corredoira et al. (2004) and Picaud & Robin (2004).

The two scale heights, z_Y and z_O , are also well determined parameters. z_Y is in good agreement with the values obtained by Robin et al. (1996) and Jurić et al. (2008) but slightly smaller than those found by López-Corredoira et al. (2002), Reid & Majewski (1993), and Chang et al. (2011). z_O is definitively smaller than the values in the literature (Robin et al. (1996), Larsen & Humphreys (2003), Jurić et al. (2008) and Chang et al. (2011)). López-Corredoira et al. (2002) determined the scale height of the sole disk in their model equal to 310 pc, which is intermediate between the values we found in our two-disks model. In this context, it is important to recall that in our model z_Y and z_O follow Eq. 3, and as consequence, any comparison with the literature should refer to the solar neighborhood values.

The scale length parameter of the spheroid, a_H , defines how well the “cusp” in star counts close to the galactic center is fitted. This cusp is conspicuous if we examine the K_S longitudinal counts at $|b| \sim 2.4^\circ$, the first “parallel” in the $N_{side}=16$ HEALPix scheme. To be able to reproduce the cusp with the spheroidal population of Eq. 5, a_H has necessarily to be small and the normalization N_{sph}/N_D large. The largest values needed for N_{sph}/N_D , however, do not exceed 0.01. The oblateness of the spheroid, κ , estimated to be ~ 0.57 , is consistent with the range of values in the literature, 0.55–0.8. We notice that since there is a correlation between this parameter and N_{sph}/N_D , both parameters should always be optimized simultaneously. Larsen & Humphreys (2003) suggest that this parameter could vary with galactocentric radius. Carollo et al. (2007) concluded that the spheroid would be better described by two subpopulations, one related to an inner bulge, with oblateness ~ 0.6 , and another related to an outer bulge, with oblateness ~ 0.9 .

A comparison of our results for the spheroid with those of Robin et al. (2012) would be interesting since this is a recent result also based on 2MASS data. Unfortunately, it is not straightforward. Those authors use additional components in their boxy bar/bulge + thicker ellipsoid structure. Besides, they express their results as maps of residuals given by $(C_M - C_{obs})/C_{obs}$ for a very fine grid with 15 arcmin separation in the region $|l| < 20^\circ$ and $|b| < 10^\circ$. One can see from their Figure 3 that only the central region, a few square degrees in size, presents residuals well in excess of 20%. However, their best fit model (case S + E in the paper) involves 15 parameters, while our description uses 7 parameters for the spheroid which are optimized *simultaneously* with the parameters that describe the rest of the Galaxy. Considering the same $20^\circ \times 10^\circ$ region, our model presents a smooth trend of overestimating the star counts for $|l| \lesssim 10^\circ$, with typical values of the residuals of $\sim 20\%$. The largest residual in the $20^\circ \times 10^\circ$ region is 0.46.

In models where the bulge follows a truncated power law (Binney et al. (1997) and Vanhollenbeke et al. (2009)), the scale length of the bulge plays a different role with respect to our a_H – it indicates, roughly, the truncation radius of the bar. For this reason we can not quantitatively compare

these scales. Similar difficulties are found in the case of the boxy-bulge of López-Corredoira et al. (2005). The HWHM of a Gaussian density profile would be 425 pc, close to our length scale, but the contribution of the boxy-bulge structure extends to larger galactocentric radii.

The parameter describing the contrast of the spiral arms, C_S , is very loosely constrained by the 2MASS data, in fact, even with the $N_{side} = 16$ grid which gives a separation of 5.6° at $|b| = 0^\circ$, the enhancement of the counts in the tangential directions mentioned at the end of section 2.3 are hardly seen. Clearly, higher resolution is needed to characterize this component. A similar conclusion was reached by Quillen (2002). We find indications that C_S is of the order of unity, roughly consistent with previous estimates from Drimmel & Spergel (2001), Grosbøl et al. (2004), Benjamin et al. (2005) and Liu et al. (2012).

The inclusion of a bar in the modeling of the data sampled with the $N_{side} = 16$ HEALPix scheme definitely improves the quality of the resulting fits, even though the limit of $K_S = 11$ and the spacing of $\Delta l = 5.6^\circ$ and $\Delta b = 2.4^\circ$ not being the best to constrain that feature. We find that the bar has a half length of ≈ 1.25 kpc, with axes ratios 1.00:0.22:0.39. The angle θ_{bar} is close to the lower limit of the values found in the literature, $\sim 12^\circ$ (López-Corredoira et al. 2000). The contrast of the bar with the ambient disks, C_{bar} , is ~ 3 . We did not find previous estimates of the latter quantity in the literature.

4.2.1. Comparison in selected lines-of-sight

Figures 7, 8 and 9 show cumulative histograms of star counts in nine sets of $\{l, b\}$ in JHK_S, respectively. We see that the largest differences happen close to the galactic plane, specially for $l \sim 300^\circ$ and $l \sim 60^\circ$. One can easily see the effects of the proximity to the Small Magellanic Cloud in the line-of-sight corresponding to $(l, b) = (300, -45)$ for magnitudes fainter than ≈ 13 . Figure 10 shows similar histograms for $|b| = 90^\circ$. Here we see that the limit magnitudes go all the way to the depth of the 2MASS catalog.

Counts along the galactic plane, or intercepting the same, use to be a *tour de force* for star counts models. Figure 11 shows the comparison between observations and model for 64 lines-of-

sight in the galactic plane, with and without the adoption of the density profile for the young disk given by Equation 4. The limit magnitude is 11 in the K_S band. For comparison, we also show the predicted counts from the Besançon model (Robin & Crézé 1986; Robin et al. 2003), obtained from the online form⁷. Since the only parameter which can be varied by the user in the online form is the extinction, we show the fit which provides the best description close to the galactic center. Figure 12 shows the observed and predicted counts along galactic latitude for $l = 0^\circ$. The largest differences are confined to the region close to the galactic plane. Again, for comparison, we show the predicted counts from the Besançon model. Comparing our counts to those from the Besançon model, one can see that our fit is slightly better.

An all sky map of the relative differences between observed and predicted counts produces a comprehensive view of the merits and limitations of a model. Fig. 13(c) shows as a figure of merit the ratio $(C_{obs} - C_M)/C_M$ obtained from the cumulative histograms up to magnitude 11. This is not very different but a little more intuitive than the figure of merit C_M/C_{obs} used by Chang et al. (2011). For reference, both the observed and model counts are presented in Figs. 13(a) and 13(b), respectively. As we can see in Fig. 13(c), the largest differences between observed and predicted counts are concentrated in the galactic plane. This is a limitation shared by all models in the literature. Our Fig. 13(c) resembles Figure 2 of Reylé et al. (2009), both presenting the differences between observations and model predictions. Although the model of Reylé et al. (2009) includes a description of a warp, not present in our model, the O-C differences are smaller in our case. The main differences between our map and that one from Reylé et al. (2009) are the locations where the galactic model does not coincide with observations. The excess of observed stars counts which they attribute to the warp is present in the outer Galaxy, while the largest excesses observed by us are close to $l \sim 300^\circ$ and $l \sim 60^\circ$.

Fig. 14 shows an all sky map of C_M/C_{obs} for a more direct comparison with the result obtained by Chang et al. (2011). Our description is better both at the center and anti-center regions.

⁷<http://model.obs-besancon.fr/>

5. Conclusions

We have used the 2MASS data to test a modified version of the model due to OL93 in the JHK_S bands. We emphasize that this study is the first attempt to determine the main parameters describing the Milky Way using the observed star counts in the whole sky, including the galactic plane.

A survey of the parameter space was done using the Markov chain Monte Carlo method, followed by attempts to better constrain the parameters via the Nested Sampling algorithm. A grid with 192 points generated by the HEALPix scheme was adopted as a baseline for sampling and provided good initial estimates for α_Y , α_O , z_Y , z_O , N_{sph}/N_D and κ . Since we expected poor results from the coarse grid considering that regions close to the galactic center and galactic plane show large gradients in star counts, finer grids were built to better sample those regions. In general, our results show a good agreement with the values of α_Y , α_O , z_Y , z_O , N_{sph}/N_D and κ found in the literature. We find that the “hole in the disk” (β radial component) shows a strong anti-correlation with α . The value of a_H found in this study describes the cusp in star counts close to the galactic center and this is the reason why it differs in scale from determinations of size for the spheroidal component found in the literature which describe larger scales. We find a moderate anti-correlation between the oblateness of the spheroid, κ , and the constant of normalization, N_{sph}/N_D . This is important and may happen in other models too. One has to have in mind that both parameters should be optimized simultaneously. There is also a definite anti-correlation between z_Y and z_O . These parameters, however, are very well defined, even with the use of a coarse grid.

Our model describes the star counts in 80% of the sky with an accuracy of better than 10%. In the remaining area, a few dozen lines-of-sight (out of 3072) show absolute residuals in excess of 20%. They are concentrated close to the plane ($|b| < 8^\circ$), specially around $l \sim 300^\circ$, $l \sim 60^\circ$ and surrounding the galactic center.

An overall view of the Galaxy according to our work suggests that it can be described by two disks with radial scales slightly shorter than those found in the literature. Only the thick disk needs a

“hole” in its inner part. The conspicuous concentration of sources in the direction of the galactic center can be described by a combination of contributions from the disks, from a spheroid with scale 400 pc, and from a bar that has aspect ratios 1.00:0.22:0.39, and is seen at an angle of 12° .

6. Acknowledgments

PFM received financial support for this work from *Coordenação de Aperfeiçoamento de Pessoal de Nível Superior*. This publication makes use of data products from the Two Micron All Sky Survey, which is a joint project of the University of Massachusetts and the Infrared Processing and Analysis Center/California Institute of Technology, funded by the National Aeronautics and Space Administration and the National Science Foundation.

REFERENCES

- Amôres, E. B., & Lépine, J. R. D. 2005, *AJ*, 130, 659
- Amôres, E. B., Lépine, J. R. D., & Mishurov, Y. N. 2009, *MNRAS*, 400, 1768
- Bahcall, J. N., & Soneira, R. M. 1980, *ApJS*, 44, 73
- Benjamin, R. A., Churchwell, E., Babler, B. L., et al. 2005, *ApJ*, 630, L149
- Bienayme, O., Robin, A. C. & Crézé, M. 1987, *A&A*, 180, 94
- Bilir, S., Cabrera-Lavers, A., Karaali, S., et al. 2008, *PASA*, 25, 69
- Binney, J. & Merrifield, M. 1998, *Galactic Astronomy* (Princeton: Princeton Univ. Press)
- Binney, J. J., Gerhard, O. E., Stark, A. A., Bally, J. & Uchida, K. I. 1991, *MNRAS*, 252, 210
- Binney, J., Gerhard, O. & Spergel, D. 1997, *MNRAS*, 288, 365
- Bissantz, N., & Gerhard, O. 2002, *MNRAS*, 330, 591
- Blitz, L., & Spergel, D. 1991, *ApJ*, 379, 631B
- Bochanski, J. J., Hawley, S. L., Covey, K. R., et al. 2010, *AJ*, 139, 2679
- Bohlin, R. C., Savage, B. D., & Drake, J. F. 1978, *ApJ*, 224, 132
- Buser, R., Rong, J., & Karaali, S. 1999, *A&A*, 348, 98
- Cabrera-Lavers, A., Bilir, S., Ak, S., Yaz, E., López-Corredoira, M. 2007, *A&A*, 464, 565
- Cabrera-Lavers, A., González-Fernández, C., Garzón, F., Hammersley, P. L. & López-Corredoira, M. 2008, *A&A*, 491, 781
- Cao, L., Mao, S., Nataf, D., Rattenbury, N. J. & Gould, A. 2013, *MNRAS*, 434, 595
- Carollo, D., Beers, T. C., Lee, Y. S., et al. 2007, *Nature*, 450, 1020
- Chang, C.-K., Ko, C.-M. & Peng, T.-H. 2010, *ApJ*, 724, 182
- Chang, C.-K., Ko, C.-M. & Peng, T.-H. 2011, *ApJ*, 740, 34
- Charbonneau, P. 1995, *ApJS*, 101, 309
- Chen, B., Stoughton, C., Smith, J. A., et al. 2001, *ApJ*, 553, 184
- Churchwell, E., Babler, B. L., Meade, M. R., et al. 2009, *PASJ*, 121, 877
- Cohen, R. J. & Few, R. W. 1976, *MNRAS*, 176, 495
- Cutri, R. M., Skrutskie, M. F., van Dyk, S., et al. 2003, *yCat*, 2246, 0
- Dame, T. M., Hartmann, D. & Thaddeus, P. 2001, *ApJ*, 547, 792
- Djorgovski, S. & Sosin, C. 1989, *ApJ*, 341, L13
- Drimmel, R. & Spergel, D. N. 2001, *ApJ*, 556, 181
- Dwek, E., Arendt, R. G., Hauser, M. G., et al. 1995, *ApJ*, 445, 716
- Elias, J. H., 1978, *AJ*, 83, 791
- Englmaier, P. & Gerhard, O. 1999, *MNRAS*, 304, 512
- Feast, M. 2000, *MNRAS*, 313, 596

- Francis, C. & Anderson, E. 2012, MNRAS, 422, 1283
- Freudenreich, H. T., Berriman, G. B., Dwek, E., et al. 1994, ApJ, 429, L69
- Freudenreich, H. T. 1998, ApJ, 492, 495
- Fux, R. 1999, A&A, 345, 787
- Fux, R., & Martinet, L. 1994, A&A, 287, L21
- Georgelin, Y. M., & Georgelin, Y. P. 1976, A&A, 49, 57
- Gilks, W., Richardson, S. & Spiegelhalter, D. 1996, Markov chain Monte Carlo in practice, Chapman & Hall
- Gilmore, G. 1984, MNRAS, 207, 223
- Gilmore, G., & Reid, N. 1983, MNRAS, 202, 1025
- Girardi, L., Groenewegen, M. A. T., Hatziminaoglou, E. & Costa, L. da. 2005, A&A, 436, 895
- Gonzalez, O. A., Rejkuba, M., Minniti, D., et al. 2011, A&A, 534, L14
- Górski, K. M., Hivon, E., Banday, A. J., et al. 2005, ApJ, 622, 759
- Grosbøl, P., Patsis, P. A. & Pompei, E. 2004, A&A, 423, 849
- Guglielmo, F. 1990, Publications de L'Observatoire de Paris
- Guglielmo, F., Le Bertre, T. & Epchtein, N. 1998, A&A, 334, 609
- Hammersley, P. L., Garzon, F., Mahoney, T. & Calbet, X. 1995, MNRAS, 273, 206
- Han, C. & Gould, A. 1995, ApJ, 449, 521
- Hernquist, L. 1990, ApJ, 356, 359
- Hou, L. G., Han, J. L. & Shi, W. B. 2009, A&A, 499, 473
- Ishida, K., & Mikami, T. 1982, PASJ, 34, 89
- Jurić, M., Ivezić, Ž., Brooks, A., et al. 2008, ApJ, 673, 864
- Larsen, J. A. & Humphreys, R. M. 2003, AJ, 125, 1958
- Lépine, J. R. D., & Leroy, P. 2000, MNRAS, 313, 263
- Lépine, J. R. D., Roman-Lopez, A., Abraham, Z., Junqueira, T. C. & Mishurov, Y. 2011, MNRAS, 414, 1607
- Levine, E. S., Blitz, L. & Heiles, C. 2006, Science, 312, 1773
- Liszt, H. S. & Burton, W. B. 1980, ApJ, 236, 779
- Liu, C., Xue, X., Fang, M., et al. 2012, ApJ, 753, L24
- López-Corredoira, M., Hammersley, P. L., Garzón, F., Simonneau, E. & Mahoney, T. J. 2000, MNRAS, 313, 392
- López-Corredoira, M., Cabrera-Lavers, A., Garzón, F. & Hammersley, P. L. 2002, A&A, 394, 883
- López-Corredoira, M., Cabrera-Lavers, A., Gerhard, O. E. & Garzón, F. 2004, A&A, 421, 953
- López-Corredoira, M., Cabrera-Lavers, A. & Gerhard, O. E. 2005, A&A, 439, 107
- López-Corredoira, M., Cabrera-Lavers, A., Mahoney, T. J., et al. 2007, AJ, 133, 154
- Majaess, D. J., Turner, D. G. & Lane, D. J. 2009, MNRAS, 398, 263
- Malkin, Z. M., 2013, Astronomy Reports, 57, 128
- Marshall, D. J., Robin, A. C., Reylé, C., Schultheis, M. & Picaud, S. 2006, A&A, 453, 635
- McClure-Griffiths, N. M., Dickey, J. M., Gaensler, B. M. & Green, A. J. 2004, ApJ, 607, L127
- McWilliam, A. & Zoccali, M. 2010, ApJ, 724, 1491
- Morris, M. R., Meyer, L., & Ghez, A. M. 2012, Research in Astronomy and Astrophysics, 12, 995
- Murray, C. A., Penston, M. J., Binney, J. J., & Houk, N. 1997, in Hipparcos - Venice '97, ESA SP-402, 485

- Nakada, Y., Onaka, T., Yamamura, I., et al. 1991, *Nature*, 353, 140
- Nataf, D. M., Gould, A., Fouqué, P., et al. 2013, *ApJ*, 769, 88
- Nelder, J. A. & Mead, R. 1965, *Computer Journal*, 7, 308
- Ojha, D. K. 2001, *MNRAS*, 322, 426
- Ortiz, R., & Lépine, J. R. D. 1993, *A&A*, 279, 90
- Peters, W. L. 1975, *ApJ*, 195, 617
- Picaud, S. & Robin, A. C. 2004, *A&A*, 428, 891
- Porcel, C., Garzon, F., Jimenez-Vicente, J., & Battaner, E. 1998, *A&A*, 330, 136
- Quillen, A. C. 2002, *AJ*, 124, 924
- Reid, M. J. 2012, in *IAU Symp. 287, Cosmic Masers - from OH to H0*, ed. R. S. Booth, W. H. T. Vlemmings & E. M. L. Humphreys (Cambridge: Cambridge Univ. Press), 359
- Reid, M. J. 2013, in *IAU Symp. 289, Advancing the Physics of Cosmic Distances*, ed. R. de Grijs (Cambridge: Cambridge Univ. Press), 188
- Reid, M. J., Menten, K. M., Zheng, X. W., Brunthaler, A. & Xu, Y. 2009, *ApJ*, 705, 1548
- Reid, N., & Majewski, S. R. 1993, *ApJ*, 409, 635
- Reid, I. N., & Gizis, J. E. 1997, *AJ*, 113, 2246
- Reylé, C., Marshall, D. J., Robin, A. C. & Schultheis, M. 2009, *A&A*, 495, 819
- Robin, A., & Crézé, M. 1986, *A&A*, 157, 71
- Robin, A. C., Haywood, M., Crézé, M., Ojha, D. K., & Bienayme, O. 1996, *A&A*, 305, 125
- Robin, A. C., Reylé, C., & Crézé, M. 2000, *A&A*, 359, 103
- Robin, A. C., Reylé, C., Derrière, S. & Picaud, S. 2003, *A&A*, 409, 523
- Robin, A. C., Marshall, D. J., Schultheis, M. & Reylé, C. 2012, *A&A*, 538, A106
- Robitaille, T. P., Churchwell, E., Benjamin, R. A., et al. 2012, *A&A*, 545, A39
- Ruelas-Mayorga, R. A. 1991, *RevMexAA*, 22, 27
- Russeil, D. 2003, *A&A*, 397, 133
- Saito, R. K., Zoccali, M., McWilliam, A., et al. 2011, *AJ*, 142, 76
- Schlegel, D. J., Finkbeiner, D. P. & Davis, M. 1998, *ApJ*, 500, 525
- Siegel, M. H., Majewski, S. R., Reid, I. N. & Thompson, I. B. 2002, *ApJ*, 578, 151
- Skilling, J. 2004, in *AIP Conf. Proc. 735, Nested Sampling*, ed. R. Fischer, R. Preuss & U. V. Toussaint (Melville, NY: AIP), 395.
- Sivia, D. & Skilling, J. 2006, *Data Analysis: a Bayesian tutorial* (2nd ed., Oxford: Oxford Univ. Press)
- Skrutskie, M. F., Cutri, R. M., Stiening, R., et al. 2006, *AJ*, 131, 1163
- Sofue, Y., Honma, M. & Omodaka, T. 2009, *PASJ*, 61, 227
- Stanek, K. Z., Mateo, M., Udalski, A., et al. 1997, *ApJ*, 477, 163
- Trumpler, R. J. 1930, *PASP*, 42, 214
- Udalski, A., Szymanski, M., Stanek, K. Z., et al. 1994, *Acta Astronomica*, 44, 165
- Vallée, J. P. 1995, *ApJ*, 454, 119
- Vallée, J. P. 2002, *ApJ*, 566, 261
- Vallée, J. P. 2005, *AJ*, 130, 569
- Vallée, J. P. 2008, *AJ*, 135, 1301
- Vanhollebeke, E., Groenewegen, M. A. T. & Girardi, L. 2009, *A&A*, 498, 95
- Wainscoat, R. J., Cohen, M., Volk, K., Walker, H. J., & Schwartz, D. E. 1992, *ApJS*, 83, 111
- Wang, Y., Zhao, H., Mao, S. & Rich, R. M. 2012, *MNRAS*, 427, 1429
- Weiland, J. L., Arendt, R. G., Berriman, G. B., et al. 1994, *ApJ*, 425, L81
- Xu, Y., Reid, M. J., Zheng, X. W. & Menten, K. M. 2006, *Science*, 311, 54

Zhao, H., Spergel, D. N. & Rich, R. M. 1995, *ApJ*,
440, L13

Zhu, Z. & Shen, M. 2013, *IAU Symposium*, 289,
444

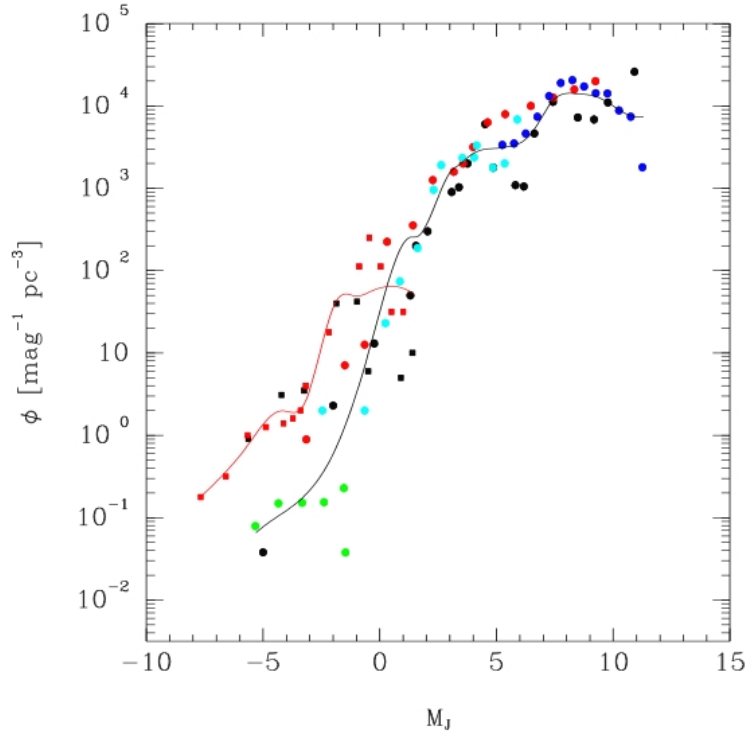


Fig. 1.— Updated luminosity functions for main sequence and giant stars in the J band. The circles and squares indicate, respectively, the main sequence and giants luminosity functions according to Ortiz & Lépine (1993) (black), Wainscoat et al. (1992) (red), Bochanski et al. (2010) (blue), Reid & Gizis (1997) (green) and Murray et al. (1997) (cyan). The lines indicate the smooth fits for the main sequence (black) and giants (red).

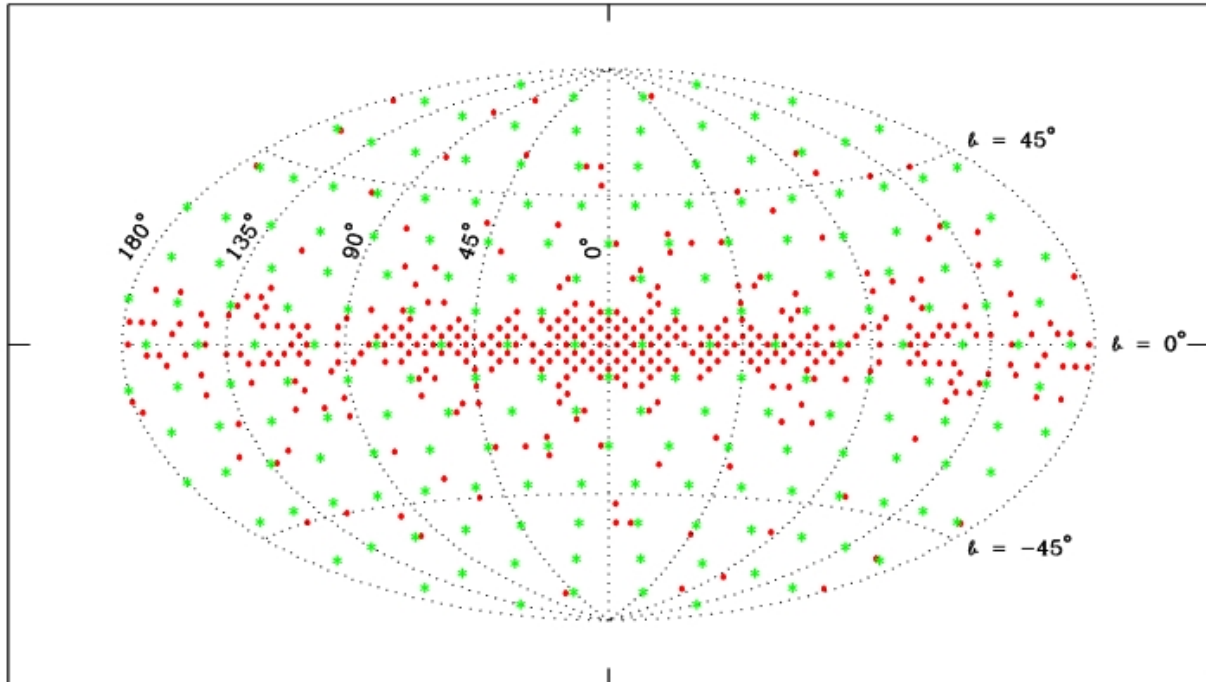


Fig. 2.— Illustration of the $N_{side}=4$ (192 points) basic grid in green and a finer grid with 382 points drawn from the $N_{side}=16$ HEALPix scheme (red).

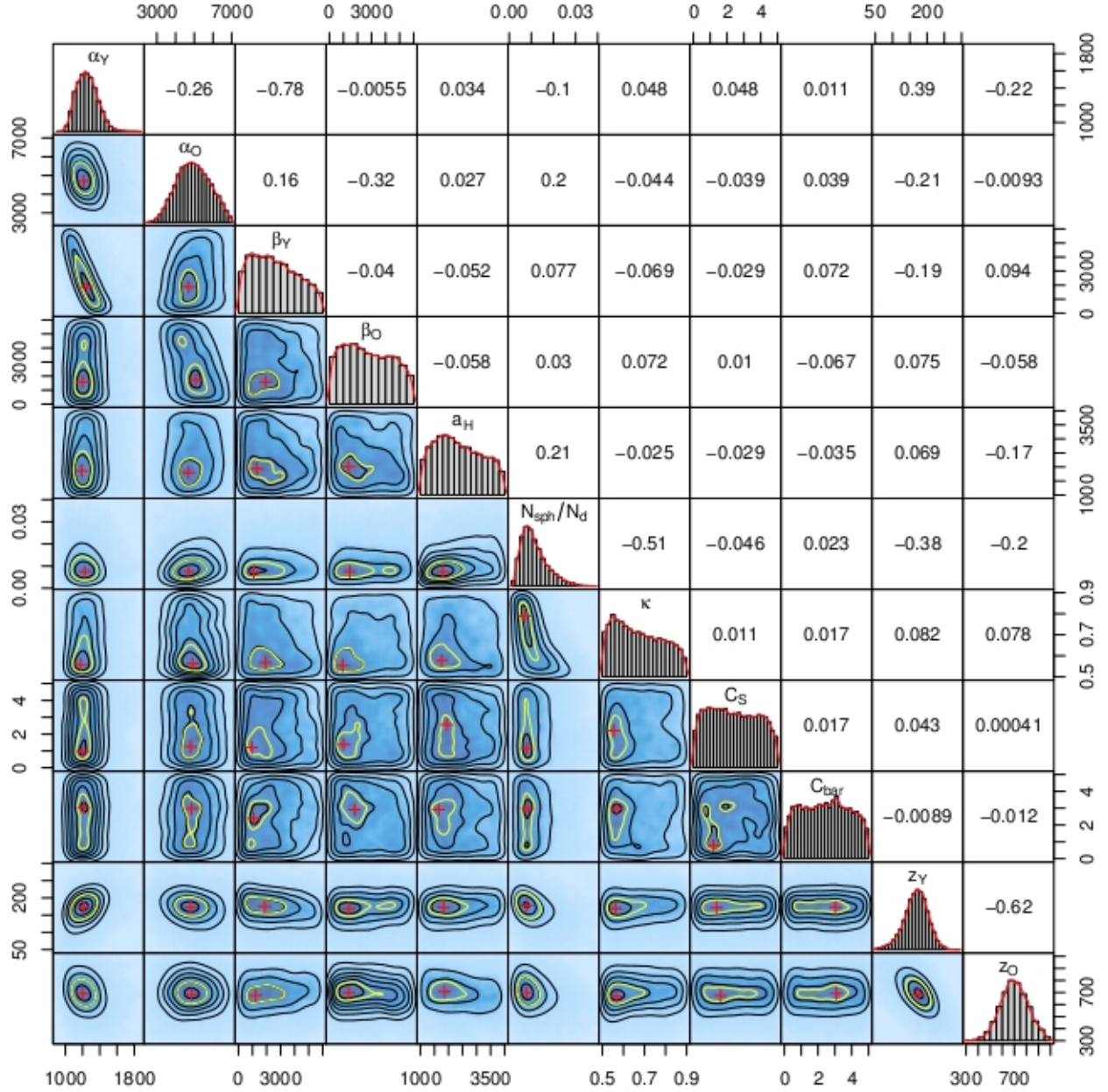


Fig. 3.— Joint *a posteriori* probability densities for the parameters of our model after 10^5 iterations of a MCMC, considering the $N_{side}=4$ grid. The marginalized 1D histograms for the parameters are displayed on the diagonal. We also included the correlation coefficients between each pair of parameters. The red cross indicates the mode of the 2D distribution and the yellow contour shows the 95% confidence region.

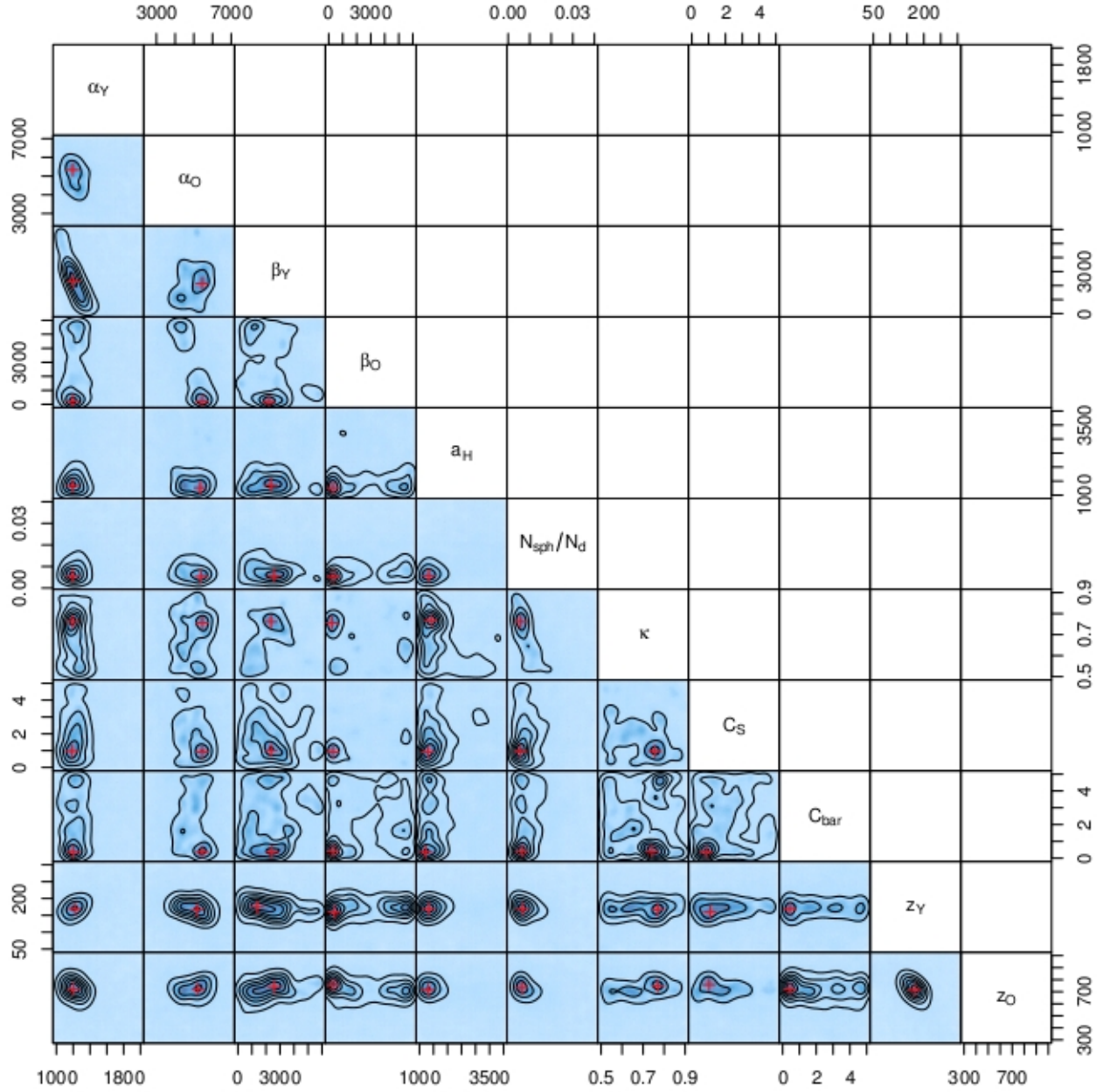


Fig. 4.— The distribution of densities for the parameters of our model after 7400 iterations of a Nested Sampling run with $N_{live} = 512$, considering the $N_{side}=4$ grid. The red symbol indicates the mode of the 2D distribution.

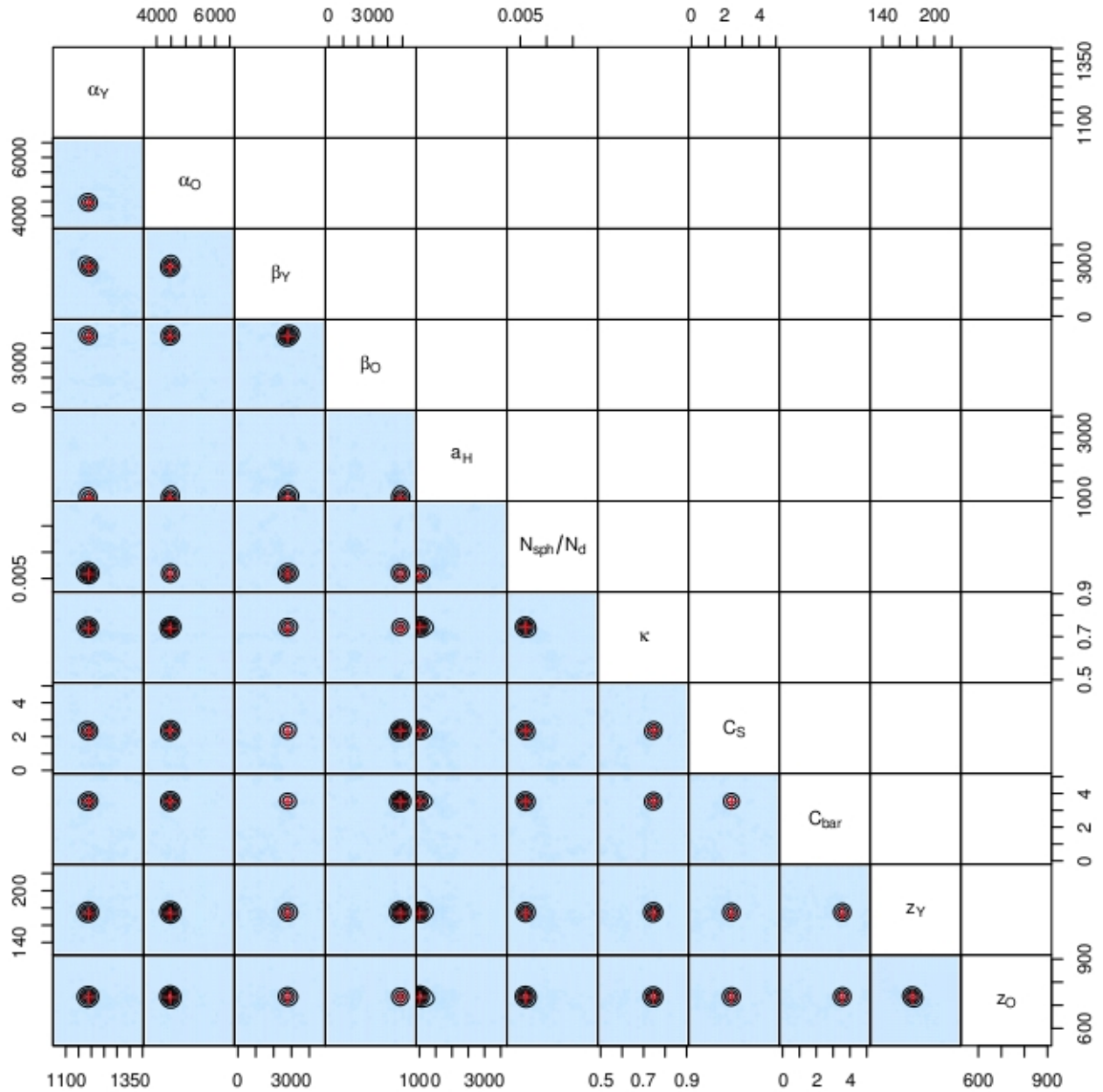


Fig. 5.— The distribution of densities for the parameters of our model from a Nested Sampling run which started with $N_{live} = 32$ random states chosen among the ones with the 5% best likelihoods in a MCMC of 25000 iterations, considering the $N_{side}=4$ grid. The red symbol indicates the mode of the 2D distribution.

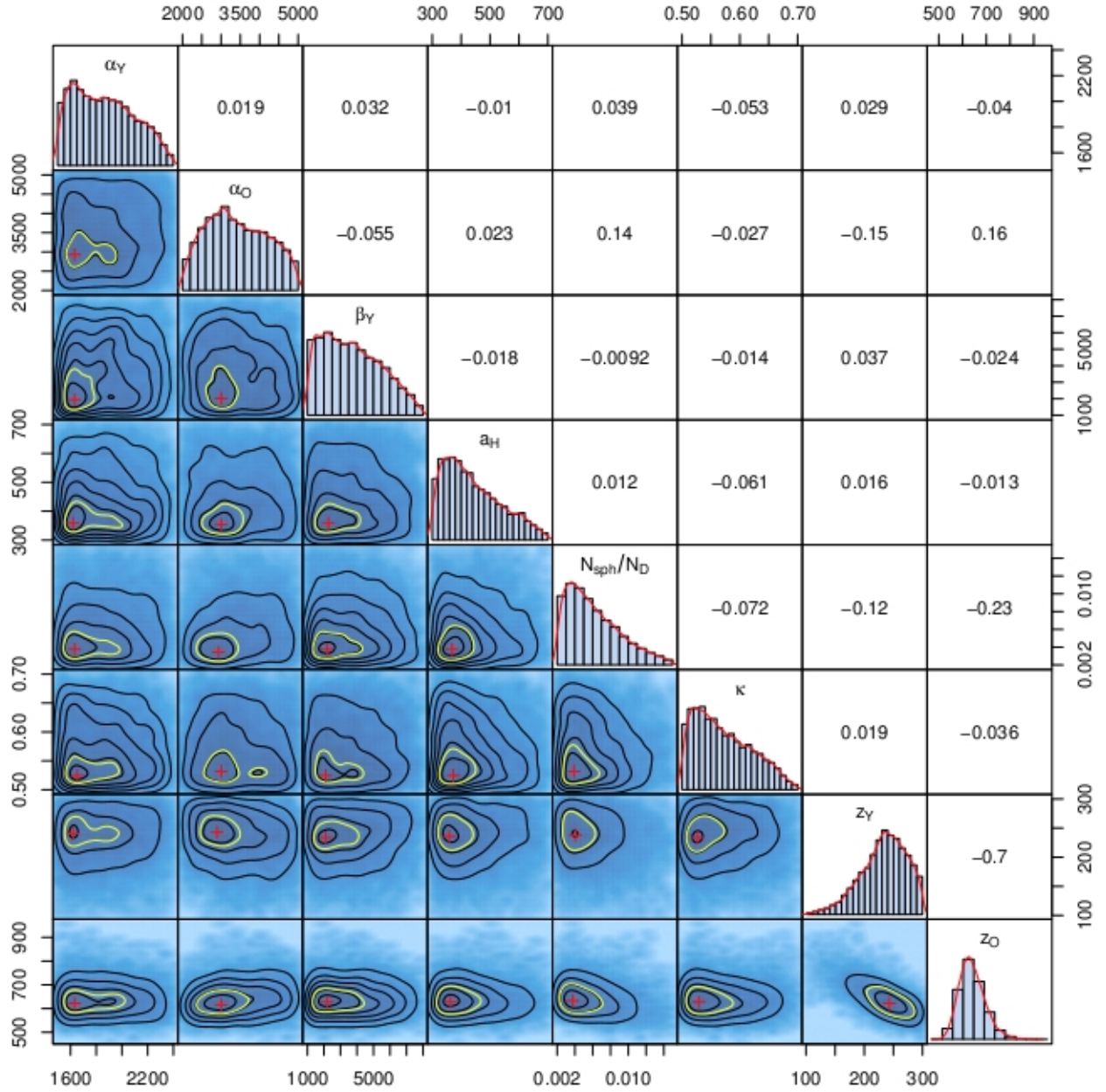


Fig. 6.— Joint *a posteriori* probability densities for the parameters of our model after 7×10^4 iterations of a MCMC, considering the finer grid of 382 points, shown in Figure 2. The marginalized 1D histograms for the parameters are displayed on the diagonal. We also included the correlation coefficients between each pair of parameters. The symbols are as in Fig. 3.

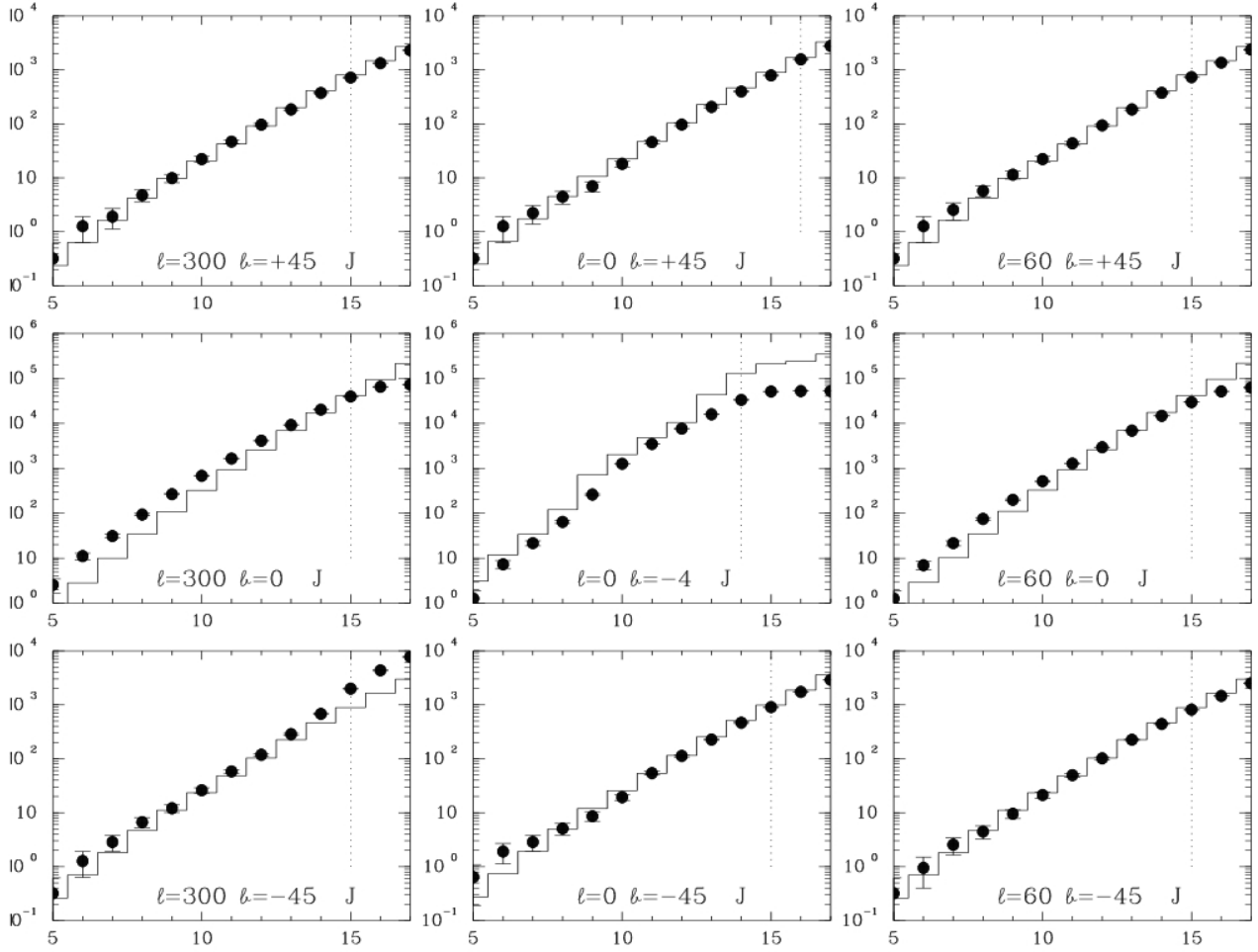


Fig. 7.— Cumulative star counts histograms for selected lines-of-sight in the J band. The filled circles with error bars represent the observations while the steps correspond to the model. The three middle histograms refer to the galactic plane or close to it, while the upper and lower histograms correspond to $|b| = 45^\circ$. The dashed line indicates the magnitude limit for each line-of-sight.

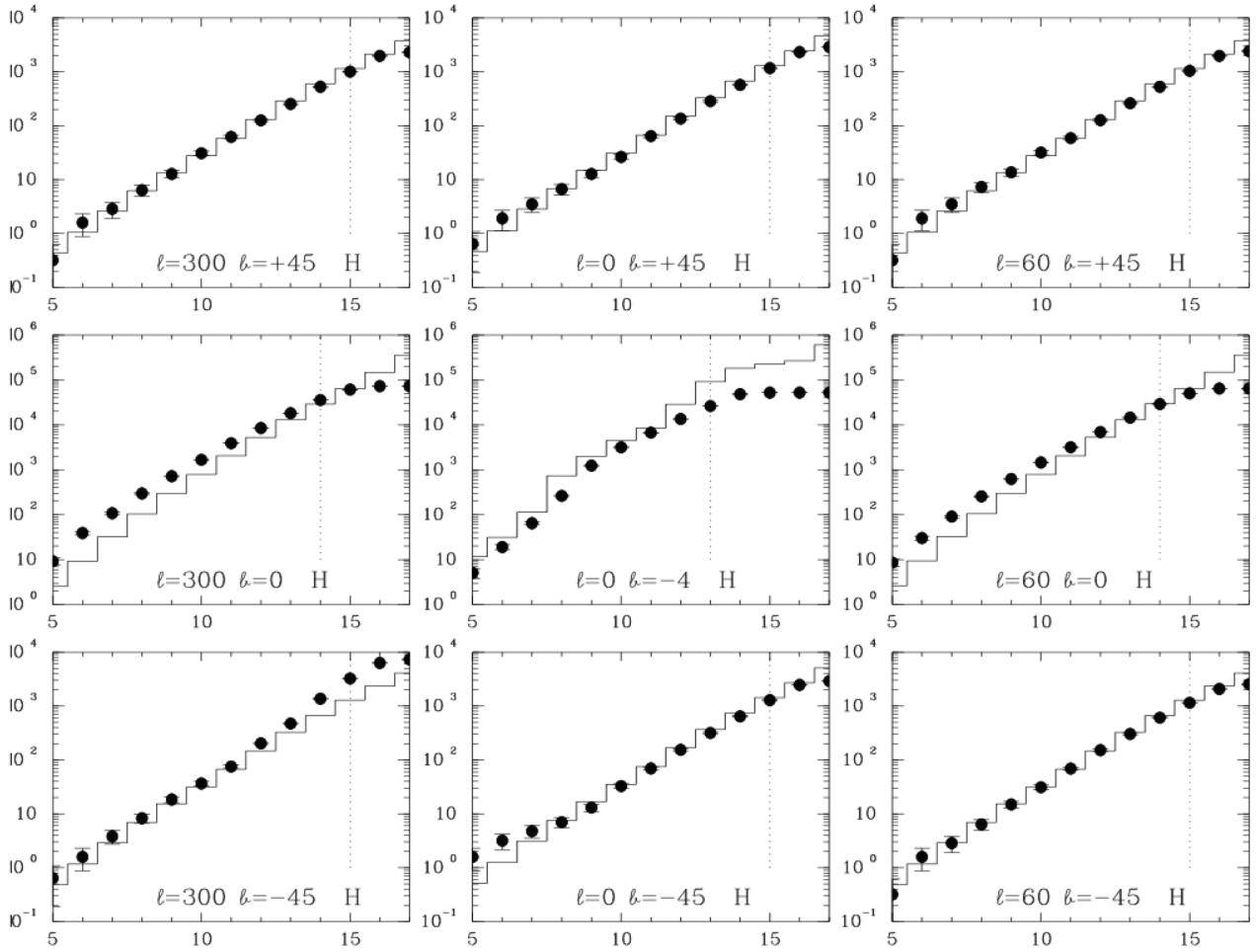


Fig. 8.— Same as Figure 7 for the H band.

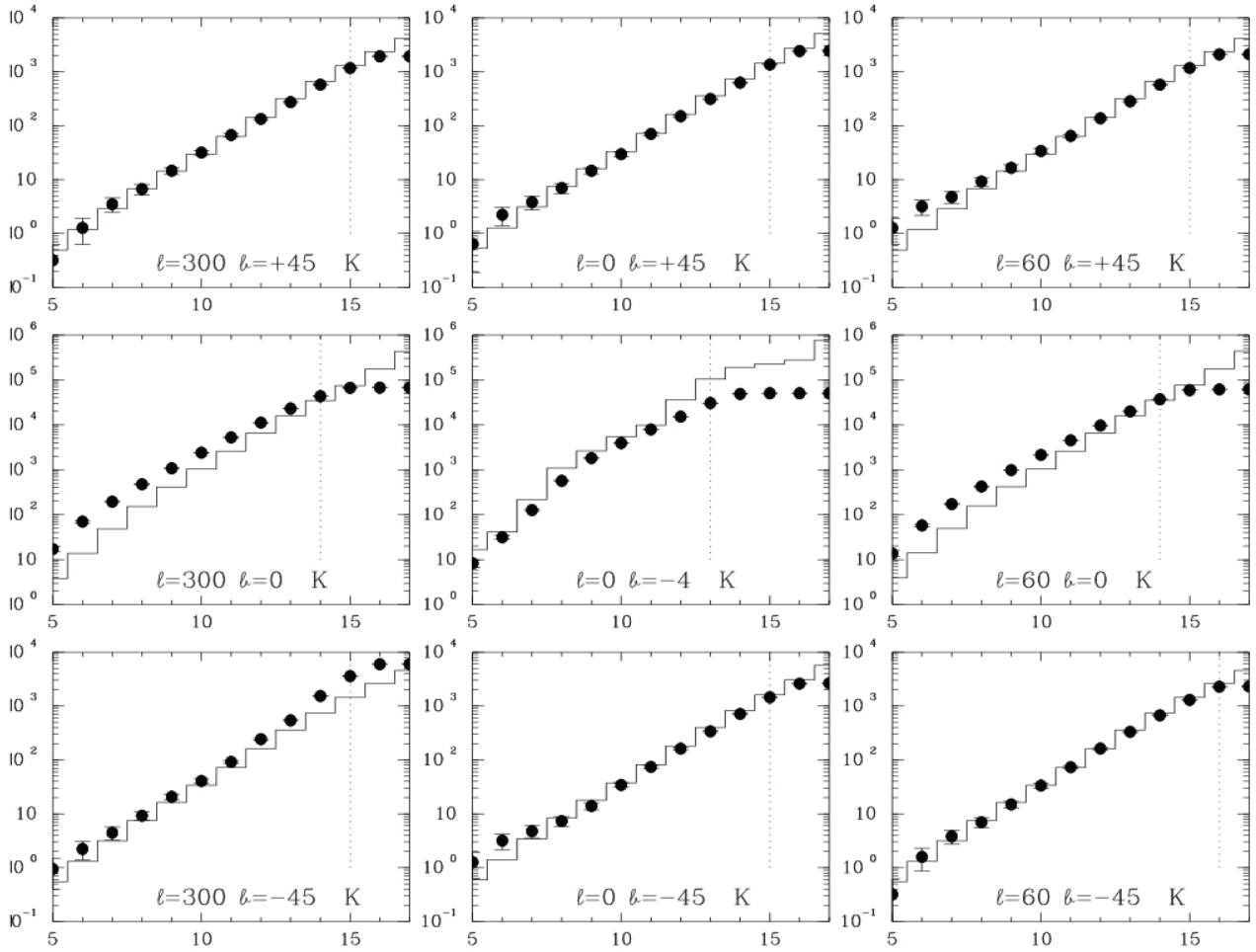


Fig. 9.— Same as Fig. 7 for the K_S band.

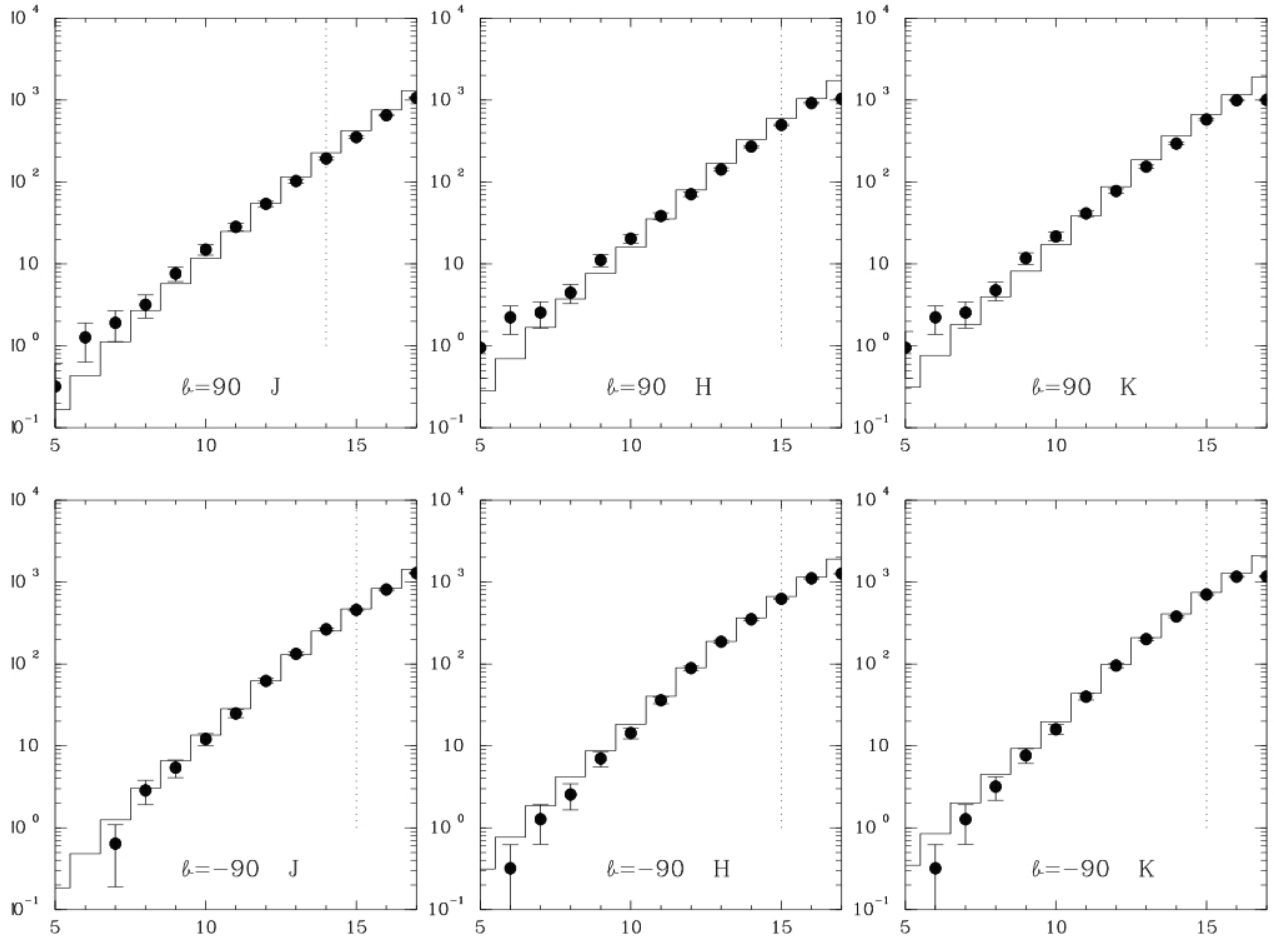


Fig. 10.— Cumulative star counts histograms for the galactic poles in JHK_S bands. Symbols are the same as in Fig. 7.

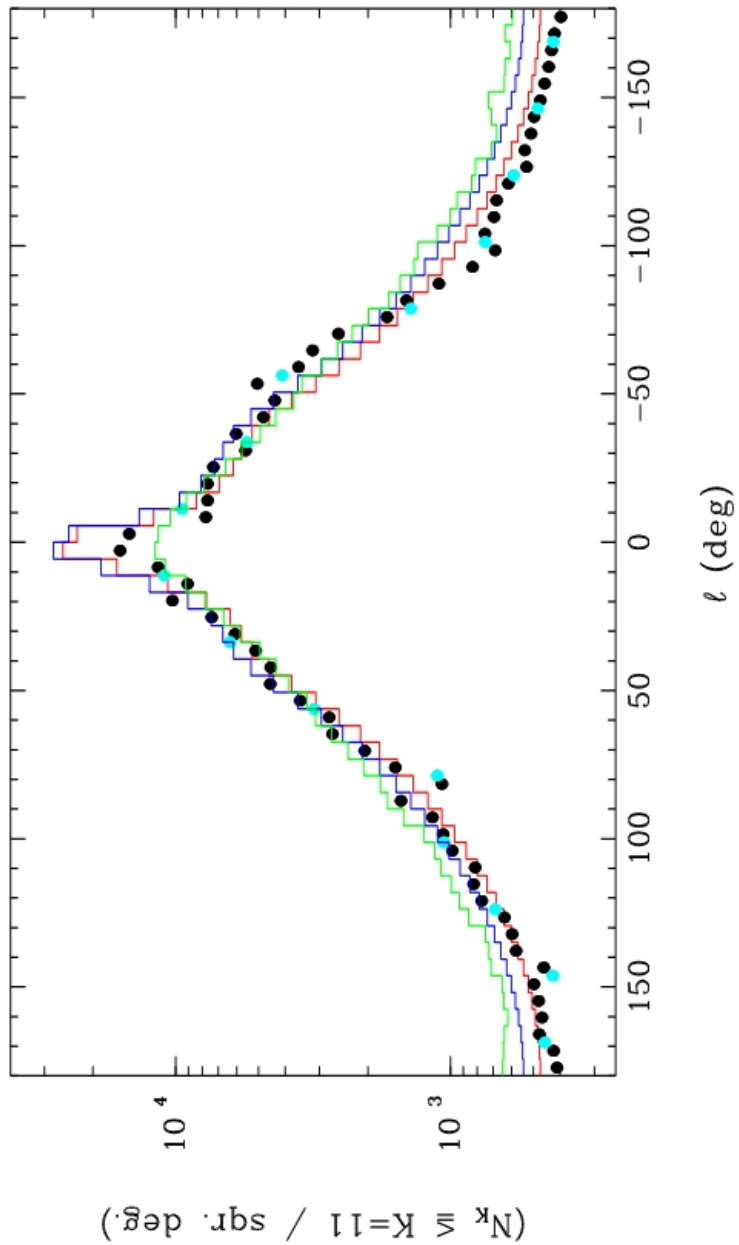


Fig. 11.— Cumulative star counts along longitude for $b = 0^\circ$ in the K_S band. The black/cyan filled circles with error bars represent the observations for the $N_{side}=4/16$ HEALPix grid. The blue and red steps correspond to the model with and without the correction of Eq. 4 for thin disk density, respectively. The green steps indicate the counts calculated with the Besançon model.

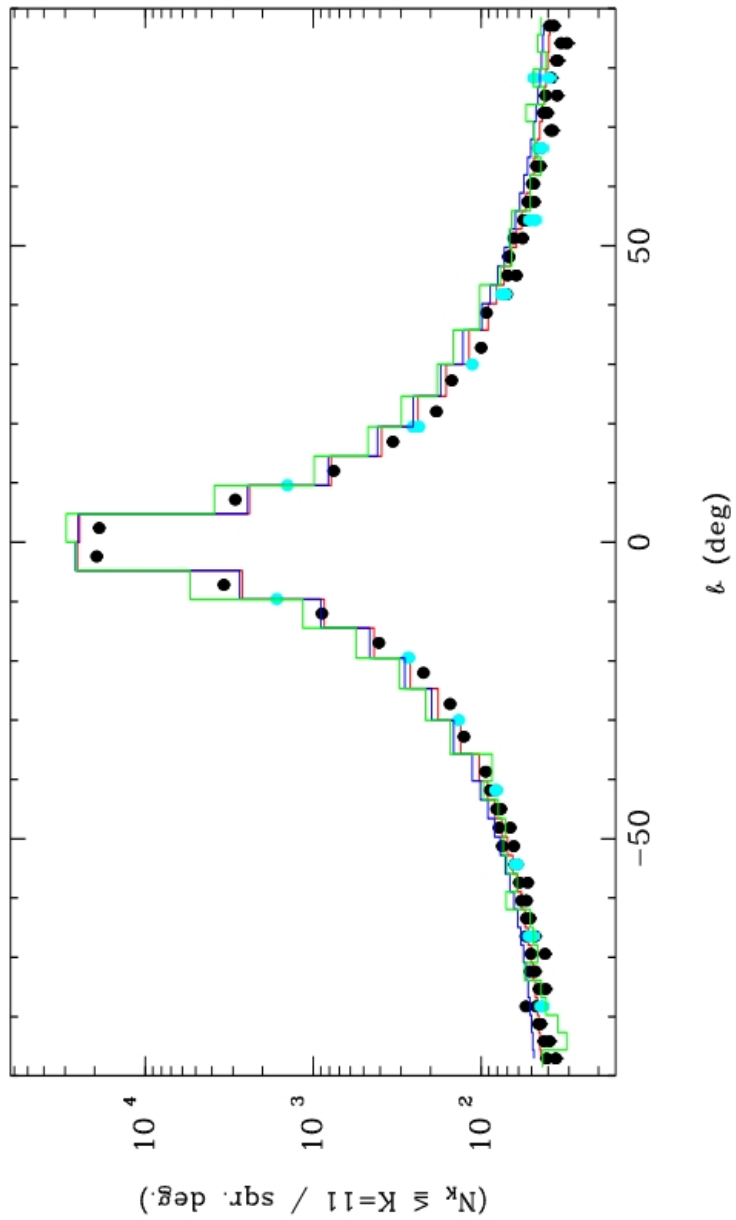


Fig. 12.— Cumulative star counts along latitude for $l = 0^\circ$ in the K_S band. The symbols are as in Fig. 10, with green steps indicating the counts calculated with the Besançon model.

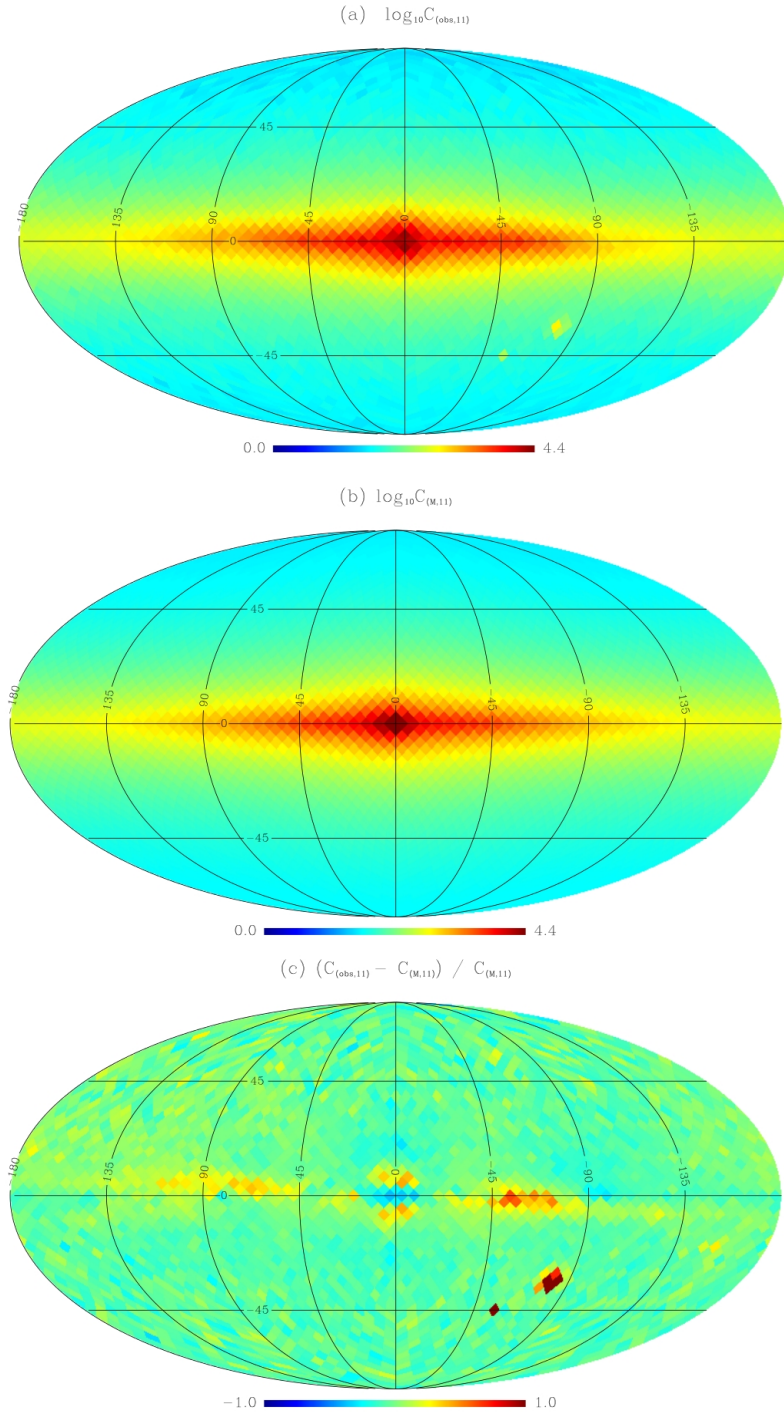


Fig. 13.— (a) The observed cumulative star counts for $K_S < 11$ sampled according to the $N_{side}=16$ HEALPix scheme (3072 grid points). Each grid point is the result of a cone search of one square degree area. The counts are color-coded in a logarithmic scale to facilitate visualization. (b) The predicted cumulative star counts from our model in the same band with the same counts coding as in (a). (c) The relative differences $(C_{(obs,11)} - C_{(M,11)}) / C_{(M,11)}$ of (a) and (b) color-coded in a *linear scale*, to emphasize the details.

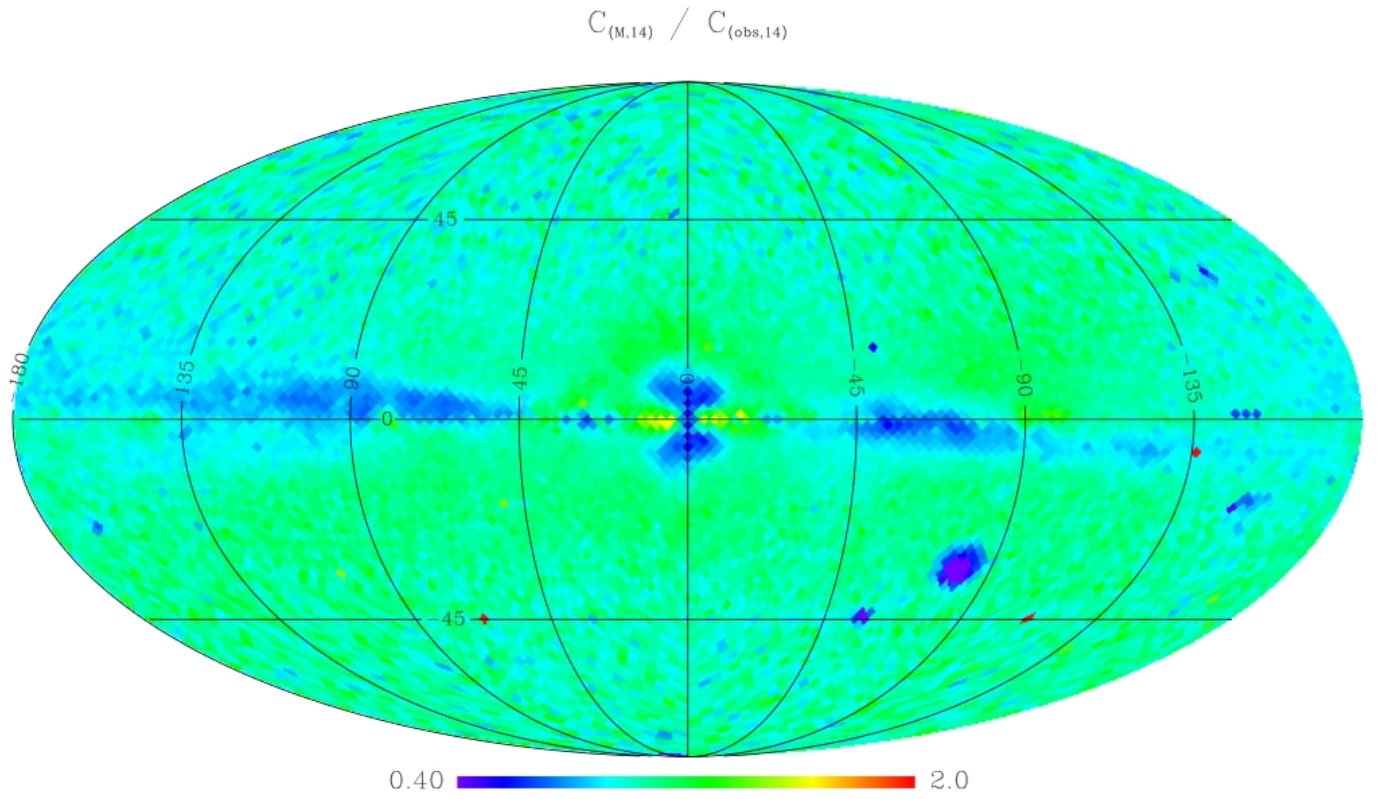


Fig. 14.— The ratio $C_{(M,14)}/C_{(obs,14)}$ in the K_S band for a 12288 grid points from the $N_{side} = 32$ HEALPix scheme, for a direct comparison with the results of Chang et al. (2011). The cumulative limiting magnitude in this case is 14.

TABLE 1
COUNTING REJECTIONS BASED ON QUALITY FLAGS.

Flag	Catalog Code	Meaning
Photometric quality	X,U ^a	Objects not detected in one of the bands or from which it was not possible to estimate the brightness
Read	0, 9 ^b	Objects not detected in one of the bands or, although detected, it was not possible to make useful estimates of brightness
Contamination and confusion	p, c, d, s, b ^c	Objects affected by the proximity of a bright source or image artifacts
Galactic contamination	1, 2 ^d	Objects contaminated by the proximity of extended sources

^aPossible codes for this flag are X, U, F, E, A, B, C, D

^bPossible codes for this flag are 0, 1, 2, 3, 4, 6, 9

^cPossible codes for this flag are p, c, d, s, b, 0

^dPossible codes for this flag are 0, 1, 2

TABLE 2
 PERCENTAGE OF REJECTIONS FOR SELECTED LINES-OF-SIGHT IN J, H AND K_S .

(l,b)	Band	$m = 9.5$	$m = 10.5$	$m = 11.5$	$m = 12.5$	$m = 13.5$
(0,+45)	J	0.0	0.0	0.5	1.6	2.9
	H	0.2	0.2	1.1	2.6	3.4
	K_S	0.1	0.0	0.2	0.3	1.8
(60,+45)	J	0.2	0.2	0.2	1.2	7.5
	H	0.4	0.6	0.2	2.6	9.4
	K_S	0.2	0.1	0.3	1.6	3.8
(300,+45)	J	0.7	0.7	0.3	2.0	3.3
	H	0.4	0.4	0.2	1.3	5.7
	K_S	0.2	0.1	0.2	0.7	2.2
(0,-4)	J	0.3	1.0	2.7	8.8	33.2
	H	1.0	2.4	6.8	22.0	53.7
	K_S	1.2	3.0	8.2	26.9	40.0
(60,0)	J	0.0	0.1	0.5	1.6	5.0
	H	0.2	0.6	1.8	5.0	15.2
	K_S	0.3	0.9	2.7	6.0	21.8
(300,0)	J	0.0	0.1	0.5	1.7	5.9
	H	0.2	0.5	1.6	5.2	16.0
	K_S	0.3	0.9	2.8	8.2	23.7
(0,-45)	J	0.0	0.4	0.2	1.1	4.4
	H	0.3	0.3	0.3	3.0	5.0
	K_S	0.1	0.1	0.4	1.4	3.0
(60,-45)	J	0.3	0.3	0.3	1.1	3.8
	H	0.2	0.2	0.2	1.9	4.2
	K_S	0.0	0.2	0.2	1.0	2.9
(300,-45)	J	0.1	0.1	0.3	0.5	3.0
	H	0.1	0.1	0.3	0.7	3.9
	K_S	0.0	0.1	0.1	0.5	2.4

TABLE 3
LIMITS FOR PARAMETERS SEARCH.

Parameter	Symbol	Lower	Upper
Radial scale length of thin/thick disks (pc)	α_Y, α_O	500	7000
Radii of the central hole in thin/thick disks (pc)	β_Y, β_O	0	6000
Length parameter of the spheroid (pc)	a_H	100	4000
Spheroid to disk density ratio	N_{sph}/N_D	0.001	0.020
Oblate spheroid parameter	κ	0.5	0.9
Density contrast of the spiral arms	C_S	0.0	3.0
Density contrast of the bar	C_{bar}	0.0	5.0
Scale height of the thin disk (pc)	z_Y	50	400
Scale height of the thick disk (pc)	z_O	200	1000
Bar half length (pc)	l_{bar}	700	4000
Orientation angle of the bar (deg)	θ_{bar}	11	53

TABLE 4
RESULTS FROM MCMC, NS AND MCMC+NS FOR THE $N_{side}=4$ HEALPIX GRID.

Parameter	MCMC	NS	MCMC+NS
α_Y (pc)	(1230^{+190}_{-170})	(1200^{+190}_{-170})	(1190^{+170}_{-160})
α_O (pc)	(4750^{+920}_{-690})	(5150^{+920}_{-690})	(4420^{+850}_{-750})
β_Y (pc)	(920^{+2570}_{-570})	(2140^{+2570}_{-570})	(2770^{+1700}_{-600})
β_O (pc)	(1740^{+2570}_{-1430})	(100^{+2570}_{-100})	(4760^{+1240}_{-730})
a_H (pc)	(1940^{+570}_{-640})	(1350^{+570}_{-640})	(1000^{+550}_{-410})
N_{sph}/N_D	$(0.0073^{+0.0064}_{-0.0036})$	$(0.0058^{+0.0064}_{-0.0036})$	$(0.0058^{+0.0072}_{-0.0033})$
κ	$(0.55^{+0.10}_{-0.05})$	$(0.76^{+0.10}_{-0.05})$	$(0.74^{+0.09}_{-0.04})$
C_S	$(0.9^{+3.3}_{-0.5})$	$(1.0^{+3.3}_{-0.5})$	$(2.3^{+1.1}_{-0.7})$
C_{bar}	$(3.0^{+0.9}_{-2.5})$	$(0.4^{+0.9}_{-0.4})$	$(3.5^{+1.5}_{-0.3})$
z_Y (pc)	(170^{+40}_{-30})	(170^{+40}_{-30})	(170^{+40}_{-40})
z_O (pc)	(680^{+120}_{-90})	(710^{+120}_{-90})	(730^{+130}_{-90})
l_{bar}^* (pc)	2000	2000	2000
θ_{bar}^* (deg)	30	30	30

*These parameters were kept fixed at the values indicated.

TABLE 5
COMPARISON BETWEEN DIFFERENT WEIGHTING SCHEMES.

Parameter	\sqrt{N}	5-points variance
α_Y (pc)	$\left(1200^{+220}_{-140}\right)$	$\left(1330^{+190}_{-190}\right)$
α_O (pc)	$\left(5150^{+520}_{-1090}\right)$	$\left(4970^{+730}_{-550}\right)$
z_Y (pc)	$\left(170^{+40}_{-30}\right)$	$\left(180^{+40}_{-30}\right)$
z_O (pc)	$\left(710^{+90}_{-120}\right)$	$\left(770^{+130}_{-60}\right)$

TABLE 6
COMPARISON WITH RESULTS IN THE LITERATURE.

Parameter	Our result	Value from literature	Source
α_Y (pc)	(2120±200)	(2500 ⁺⁸⁰⁰ ₋₆₀₀)	Fux & Martinet (1994)
		2600	Freudenreich (1998)
		(2100±300)	Porcel et al. (1998)
		(3300±600)	Feast (2000)
		1700	Lépine & Leroy (2000)
		(2800±300)	Ojha (2001)
		(2100 ⁺²²⁰ ₋₁₇₀)	López-Corredoira et al. (2002)
		(3500±300)	Larsen & Humphreys (2003)
		2400	Picaud & Robin (2004)
		(2600±520)	Jurić et al. (2008)
		2200	Reylé et al. (2009)
		(3700±1000)	Chang et al. (2011)
		3500	Reid & Majewski (1993)
		(2800±800)	Robin et al. (1996)
α_O (pc)	(3050±500)	(3000±1500)	Buser et al. (1999)
		2300	Lépine & Leroy (2000)
		(3700±800)	Ojha (2001)
		(4700±200)	Larsen & Humphreys (2003)
		(3600±720)	Jurić et al. (2008)
		(5000±1000)	Chang et al. (2011)
		3000	Freudenreich (1998)
		2600	Lépine & Leroy (2000)
		2000 - 4000	López-Corredoira et al. (2004)
		(1310±1030)	Picaud & Robin (2004)
β_Y (pc)	(2070 ⁺²⁰⁰⁰ ₋₈₀₀)	325	Reid & Majewski (1993)
		250-270	Robin et al. (1996)
		100	Lépine & Leroy (2000)
		(310 ⁺⁶⁰ ₋₄₅)	López-Corredoira et al. (2002)
		(245±49)	Jurić et al. (2008)
		(360±10)	Chang et al. (2011)
		1400-1600	Reid & Majewski (1993)
		760	Robin et al. (1996)
		390	Lépine & Leroy (2000)
		900	Larsen & Humphreys (2003)
z_Y (pc)	(205±40)	(900±180)	Jurić et al. (2008)
		(1020±30)	Chang et al. (2011)
		3000	Gilmore (1984)
		2670	Reid & Majewski (1993)
		1900 ^{*,a}	Binney et al. (1997)
		420	Lépine & Leroy (2000)
		(4300±700)	Larsen & Humphreys (2003)
		(2500 ⁺¹⁷³⁰ ₋₁₆₀) ^{*,b}	Vanhollebeke et al. (2009)
		0.00125	Bahcall & Soneira (1980)
		0.0083	Guglielmo (1990)
z_O (pc)	(640±70)	0.00358	Ruelas-Mayorga (1991)
		(0.002-0.003)	Larsen & Humphreys (2003)
		0.0051	Jurić et al. (2008)
		(0.002±0.001)	Chang et al. (2011)
		(0.80±0.05)	Reid & Majewski (1993)
		0.8	Lépine & Leroy (2000)
		0.6	Robin et al. (2000)
		(0.55±0.06)	Chen et al. (2001)
		(0.65±0.05)	Girardi et al. (2005)
		(0.64±0.01)	Jurić et al. (2008)
a_H (pc)	(400±100)	1.32	Drimmel & Spergel (2001)
		1.2 - 1.4	Grosbøl et al. (2004)
		1.30	Benjamin et al. (2005)
		1.3 - 1.5	Liu et al. (2012)
N_{sph}/N_D	(0.0082±0.0030)	0.00125	Bahcall & Soneira (1980)
		0.0083	Guglielmo (1990)
		0.00358	Ruelas-Mayorga (1991)
		(0.002-0.003)	Larsen & Humphreys (2003)
		0.0051	Jurić et al. (2008)
		(0.002±0.001)	Chang et al. (2011)
		(0.80±0.05)	Reid & Majewski (1993)
		0.8	Lépine & Leroy (2000)
		0.6	Robin et al. (2000)
		(0.55±0.06)	Chen et al. (2001)
(0.65±0.05)	Girardi et al. (2005)		
κ	(0.57±0.05)	(0.64±0.01)	Jurić et al. (2008)
		1.32	Drimmel & Spergel (2001)
		1.2 - 1.4	Grosbøl et al. (2004)
C_S	(2.0 ^{+0.6} _{-0.8})	1.30	Benjamin et al. (2005)
		1.3 - 1.5	Liu et al. (2012)
		1.32	Drimmel & Spergel (2001)
C_{bar}	(3.4 ^{+1.0} _{-1.5})	1.32	Drimmel & Spergel (2001)
		1.2 - 1.4	Grosbøl et al. (2004)

TABLE 6—*Continued*

Parameter	Our result	Value from literature	Source		
l_{bar} (pc)	(1250^{+500}_{-250})	1610 – 2030	Dwek et al. (1995)		
		900	Stanek et al. (1997)		
		< 3128	Freudenreich (1998)		
		1750	Bissantz & Gerhard (2002)		
		3900	López-Corredoira et al. (2007)		
		~ 1250	Gonzalez et al. (2011)		
		~ 1460	Robin et al. (2012)		
		~ 1490	Wang et al. (2012)		
		~ 680	Cao et al. (2013)		
		θ_{bar} (deg)	(12^{+15}_{-1})	(20±10)	Dwek et al. (1995)
				20 – 30	Stanek et al. (1997)
				~ 14	Freudenreich (1998)
				12	López-Corredoira et al. (2000)
15 – 30	Bissantz & Gerhard (2002)				
20 – 35	López-Corredoira et al. (2005)				
43	López-Corredoira et al. (2007)				
(42.44±2.14)	Cabrera-Lavers et al. (2008)				
$(15^{+12.7}_{-13.3})$	Vanhollebeke et al. (2009)				
~ 30	Gonzalez et al. (2011)				
25 – 27	Nataf et al. (2013)				
13	Robin et al. (2012)				
20	Wang et al. (2012)				
29 – 32	Cao et al. (2013)				

*Bulge following a truncated power law.

^aAxis ratio 1.0:0.6:0.4 and angle between the Sun-center line and the major axis of the bulge ~ 20°.

^bAxis ratio $1.00:0.68^{+0.19}_{-0.05}:0.31^{0.04}_{-0.06}$ and angle between the Sun-center line and the major axis of the bulge $(15^{+12.7}_{-13.3})$ deg.